THESIS FOR THE DEGREE OF LICENTIATE OF ENGINEERING

Advances in Accident Tolerant Fuel Research by Doping of Uranium Nitride

Luis G. Gonzalez F.

Nuclear Chemistry

Department of Chemistry and Chemical Engineering

CHALMERS UNIVERSITY OF TECHNOLOGY

Gothenburg, Sweden 2020

Advances in Accident Tolerant Fuel Research by Doping of Uranium Nitride
Luis G. Gonzalez F.

Technical report no 2020:12

Department of Chemistry and Chemical Engineering
Chalmers University of Technology
SE-412 96 Gothenburg
Sweden
Telephone + 46 (0)31-772 1000

Cover: A chromium-doped uranium nitride microsphere showing Cr precipitation.

Chalmers Reproservice
Gothenburg, Sweden 2020

Advances in Accident Tolerant Fuel Research by Doping of Uranium Nitride

Luis G. Gonzalez F.

Nuclear Chemistry

Department of Chemistry and Chemical Engineering

Chalmers University of Technology

Abstract

Nuclear energy is a carbon-free energy source alternative often considered less harmful to the environment than fossil fuels. However, accidents have shown that there are some safety concerns regarding nuclear energy that need to be assessed before it can be considered completely safe. The loss of cooling systems during the nuclear accident at Fukushima nuclear accident exposed the flaws of the fuel used today, UO_2 encapsulated in a Zr alloy. Research into new types of improved fuels, also known as Accident Tolerant Fuels (ATF), has therefore became of great importance. Different alternative claddings and fuel materials have been explored in recent years. Amongst these, uranium nitride (UN) has shown to have very attractive thermomechanical properties. Nonetheless, UN reacts readily in oxidizing environments, making it undesirable for water-cooled reactors.

In this study, UN microspheres were manufactured through a sol-gel method, followed by carbothermic reduction and nitridation. The as-produced microspheres were pressed and sintered into pellets using spark plasma sintering (SPS). It was seen that the spherical shape was lost during sintering and densities between 77 and 98% of theoretical density were obtained, depending on the sintering parameters. For example, sintering at 1650 °C and 75 MPa for at least 5 minutes proved to produce pellets with densities close to 95% of theoretical densities, which are similar to densities used today in nuclear reactors.

Thorium and chromium were introduced as additives to form a protective oxide scale and improve the oxidation resistance of UN. It was seen that Th produced a homogeneous solid solution with uranium nitride between 0 and 20 % thorium molar metal ratio. Chromium, on the other hand, showed that there was a solubility limit in UN, and precipitation of a Cr-rich phase was observed. During exposure in air, the doped materials seem to reduce the oxidation kinetics, increasing onset temperatures and decreasing the reaction rates. Pellet exposure to water at high temperatures showed that pellets can survive at 100 °C and 1 bar pressure with zero mass change. However, at higher temperatures and pressures, 200 °C and 15 bar or 300 °C and 85 bar, pellet disintegration into a UO_2 powder was observed. An incomplete reaction was also observed for the Th-doped pellet in the exposure test at 200 °C, indicating that no improvement in the corrosion resistance of UN in water was achieved by doping with thorium.

Keywords: Uranium nitride, microspheres, doping, sintering, density, internal gelation, ATF, waterproofing.

List of Publications and Manuscripts

This thesis is based on the following paper and manuscript:

Paper I

L.G. Gonzalez Fonseca, M. Hedberg, L. Huan, P. Olsson, T. Retegan Vollmer, Application of SPS in the fabrication of UN and (U,Th)N pellets from microspheres, J. Nucl. Mater. 536 (2020) 152181. doi:10.1016/j.jnucmat.2020.152181

Contribution: Main author and most experimental work.

Paper II

L.G. Gonzalez Fonseca, M. Hedberg, T. Retegan Vollmer, Oxidation and hydrolysis of UN and (U,Th)N fuels for use as ATF. Manuscript. To be submitted by the end of September.

Contribution: Main author and all experimental work.

Abbreviations.

ATF – Accident Tolerant Fuel

BET – Brunauer-Emmett-Teller

BWR – Boiling Water Reactors

EDX – Energy Dispersive X-ray spectroscopy.

FCC – Face Centered Cubic

HMTA – HexaMethyleneTetraAmine

ICP-MS – Inductively Coupled Plasma-Mass Spectrometry

IGP – Internal Gelation Process

LOCA – Loss of Coolant Accident

LWR – Light Water Reactor

ORNL – Oak Ridge National Laboratory

PWR – Pressurized Water Reactor

SEM – Scanning Electron Microscopy

SPS – Spark Plasma Sintering

TD – Theoretical Density

TGA – Thermo-Gravimetric Analysis

UNH – Uranyl Nitrate Hexahydrate

XRD – X-Ray Diffraction

Table of contents

1. Introduction

Electricity plays a major role in modern life, from illumination to making industries run. The world's electricity consumption has increased steadily over the past several decades, and projections indicate an even larger consumption in the upcoming years [1]. Today, electric energy can be generated from different sources, such as burning fossil fuels, wind, water, and nuclear energy. For example, 64% of electricity is produced by burning fossil materials, namely coal, natural gas, and oil [1]. The release of CO_2 produced through the combustion of such fuels is known to generate environmental problems such as global warming and ocean acidification [2]. The consensus is therefore to decrease the proportion of energy produced by burning fossil fuels and incentivize more sustainable processes with lower carbon emissions.

Nuclear power became a popular energy source due to its very low carbon dioxide emissions and the high energy density of the fuel used. In early 2019, there were 451 power-producing nuclear reactors in operation worldwide. These reactors produced 2562.8 TW(e)h of electrical energy in 2019, which corresponded to 10% of the total electricity produced in the world [3]. Every energy source has its limitations, and nuclear power is no exception. One of them is the limited, although not small, amount of uranium in the earth that can be extracted at a reasonable price [4]. Due to the long-lived radionuclides produced when the fuel is burned, nuclear waste must be stored for long periods of time. As of today, deep geological disposal is the most accepted option for nuclear waste management, with some projects being under construction, for example in Finland [5].

Public opinion regarding nuclear power has been negatively impacted by the release of large amounts of radioactivity to the environment in the few accidents that have occurred in the past decades. The most recent nuclear accident occurred in 2011, in the Fukushima nuclear power plant in Japan. Fukushima's reactors are classified as pressurized water reactors (PWR), the most common type of nuclear reactors in the world [6], equipped with multiple safeguards to prevent nuclear accidents. However, a magnitude 9.0 earthquake caused a tsunami with very high waves. The power plant was not prepared for the scale of the events, and the damage to the electricity lines and backup generators caused a station blackout [7]. Due to the loss of power, and despite the efforts of the power plant operators, it was not possible to cool down the fuel. The reactor core temperature and pressure kept rising, resulting in the explosion of three reactor units. Fuels used today in PWRs are comprised of uranium dioxide (UO_2) pellets enriched with the fissile isotope ^{235}U. There are some limitations in the use of UO_2. For example, the low thermal conductivity of UO_2 has been known to affect heat transfer, and it is why the center of the pellet can reach over 2000 °C during normal operations [8]. In accidents where the cooling systems are malfunctioning, such as in the Fukushima accident, the pellet centerline temperature can reach the melting point (~2900 °C) and cause severe damage to the reactor's components.

It has been suggested that new types of fuels must be developed to withstand temperatures normally observed during accidents for longer periods of time. Such fuels are referred to as Accident Tolerant Fuels (ATF). Uranium nitride (UN) is an example of an ATF alternative proposed to be able to replace UO_2 in the future [9]. However, implementation of this ATF is not yet possible due to its incompatibility with water, the coolant used in most reactors [10]. This work is therefore aimed at developing, manufacturing and testing an ATF concept to improve the corrosion resistance of the uranium nitride fuel using thorium or chromium as

metal additives. Additionally, the manufactured fuel pellets are expected to be able to withstand interaction with water at high temperatures and pressures without losing pellet integrity.

2. Background

2.1. Nuclear accidents

Nuclear reactors are built with many safety systems to ensure safe control and management of radioactive materials during normal operations [11]. Such systems have been improved over the years, however, there is always a possibility that something unexpected can cause severe damage to the reactor, resulting in a nuclear accident. There have been only a few severe accidents in the history of nuclear power, but because of their severe impact on the environment and public safety, they have received great attention by the public and the media [12]. One of the most known nuclear disasters occurred in the Chernobyl nuclear power plant in 1986, which caused the release of several TBq of radioactivity to the environment after the explosion of its core. Its effects could be measured all around Europe [13]. The Fukushima Daiichi accident in 2011 showed that the most commonly used fuel, UO_2 pellets encapsulated in a Zr cladding, is not completely accident-proof. Due to its low thermal conductivity, UO_2 will continue to heat up in case of coolant loss, causing the fuel to melt [14]. Furthermore, at such high temperatures, the cladding undergoes a phase transformation that decreases its stability and starts to oxidize in contact with water. This results in the release of large amounts of hydrogen gas, which is what was responsible for the explosion observed in Fukushima reactor units 1, 3 and 4 [15].

2.2. Accident Tolerant Fuels

After a severe nuclear accident occurs, changes must be implemented to prevent them from recurring. During the Fukushima accident, the loss of coolant caused the production of large amounts of hydrogen due to oxidation of the zirconium cladding [16]. Design and research therefore focused on modifying the fuel elements so that they can withstand higher temperatures for longer periods with more controlled oxidation kinetics than the fuels used currently [17]. Such improved fuels, also known as ATF, must also possess the same or improved properties compared to the current fuels: [18]

1. The cladding should feature reduced oxidation kinetics while reducing the heat of oxidation in steam.
2. It should also reduce the hydrogen production rate during normal operation.
3. An alternative cladding should reduce the vulnerability to fracture and increase the resistance to thermal shock and melting.
4. An alternative fuel should possess higher thermal conductivity, reduce operating temperatures, present lesser reaction with the cladding, and increase the melting point.
5. An alternative fuel cladding system should enhance the retention of fission products during accident conditions.

Several options have been discussed previously, from slight modifications to the Zr cladding to the development of totally new fuel systems. The first studies focused on finding an alternative cladding to prevent or reduce hydrogen production [19–21]. However, it was found that such cladding will usually have a higher neutron absorption due to the use of other elements, such as iron or chromium. Some examples of alternative cladding include:

Chromium, aluminum, and molybdenum-coated Zircaloy, silicon carbide cladding, and iron-based cladding.

The other focus has been the fabrication of more advanced fuels, for example to increase the uranium molar fraction or improve the thermomechanical properties of the material by modifying the uranium matrix. UN and U_3Si_2 are two examples of these types of fuel. Other fissile material besides uranium, such as plutonium or thorium, have been studied as well, however, to a lesser extent [17,22]. Some physical properties of a few ATF candidates proposed to date are listed and compared to the standard UO_2 in Table 1. Uranium-molybdenum metallic fuels show the highest thermal conductivity out of all the candidates, which is an order of magnitude higher than for UO_2. However, it also has the lowest melting point. This fuel was designed using an annular concept in which the inner part would retain the fission products while the outer surface is enriched with aluminum, chromium, and niobium to reduce the corrosion in contact with hot water (340 °C) [23]. Uranium silicides were proposed due to their higher irradiation stability (lower swelling) in addition to their higher thermal conductivity [24]. Uranium carbide has been studied due to its improved thermal properties and uranium density in the fuel. However, its stability in water and oxygen environments is fairly poor and tends to react and oxidize easily [25]. Lastly, UN is a fuel analogous to UC, with improved thermal properties, higher heavy metal density, and slightly better oxidation resistance in air [23,26], although it is still poor compared to UO_2. Composites of these fuels, such as UN-U_3Si_2, have also been proposed to alleviate some of the drawbacks observed in the pure fuel candidates [18,27,28].

Table 1. Thermophysical properties of different uranium-based ATF candidates.

Fuel	Thermal conductivity (W/mK)	Melting point (°C)	Peak centerline temperature (°C)*	Density (g/cm^3)	Uranium density (g/cm^3)
UO_2	6-2.5 [18]	2875 [29]	2525 [8]	10.96 [29]	9.7[29]
UC	12.6-16 [30]	2495 [31]	700-1300 [30]	13.63 [31]	13.0[29]
UN	19-25 [32]	2630 [29]	930 [8]	14.32 [29]	13.5[29]
U_3Si_2	15-27.5 [33]	1665 [29]	960 [34]	12.2 [33]	11.3[33]
U-10Mo	20-37.4 [35]	1147[35]	-	17.2[35]	16.9[35]

*Peak centerline temperatures depend on the burn up of the fuel.

The main advantage of these fuel candidates, other than the higher fuel density, is the improvement in the thermal conductivity compared to UO_2. As observed in Figure 1, the thermal conductivity of the ATF candidates increases as the temperature increases, opposite of what is observed for the oxide. The thermal conductivity affects how fast the heat is distributed inside the material. An increase in the thermal conductivity will lower the peak centerline temperature of the pellets during normal operation, while also decreasing the energy stored per unit mass [36]. Table 1 also shows that the peak centerline temperature for UN and UC can vary between 700 and 1300 °C, a significant decrease compared to the 2525 °C for UO_2. In the case of a loss of coolant accident (LOCA), the margin to the melting point will therefore be larger for the ATFs.

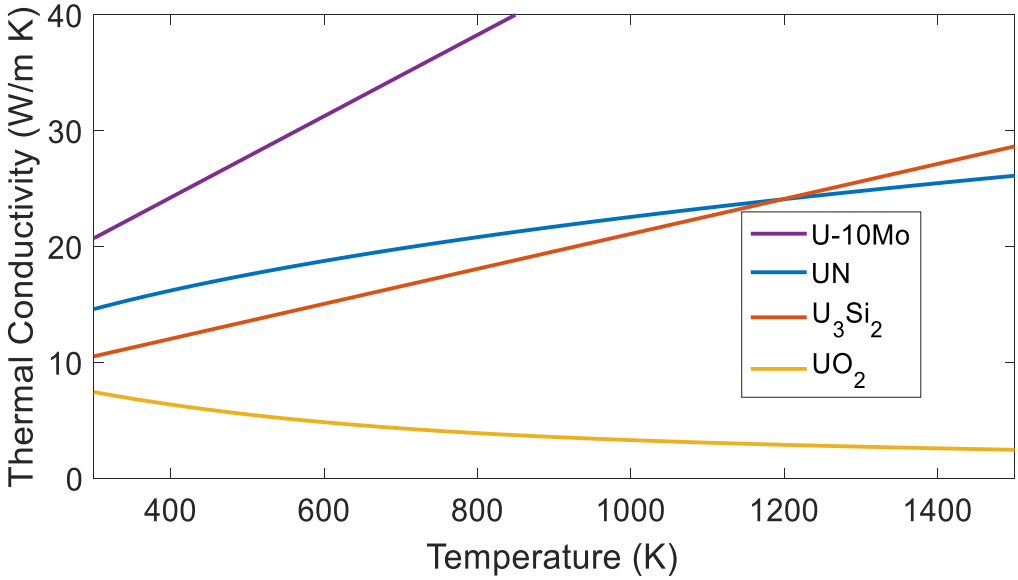

Figure 1. Thermal conductivity as a function of temperature for some ATF concepts: UN [32], *U_3Si_2* [37], *and U-10Mo* [35] *compared to the reference UO_2*[33].

2.3. Uranium Nitride

The aforementioned properties of uranium nitride suggest that it could be considered an attractive high-performance fuel. However, this alone does not mean that it can be used in the nuclear industry. Various parameters must be met by the fuel before it can be introduced as a replacement for UO_2. For example, irradiation behavior, production costs, possible revenues, and adaptation to previous technologies, are all additional criteria that must be taken into consideration. The higher uranium density present in the UN means that more fissile material can be loaded in the system. This will improve utilization of the fuel, which could then extend the fuel cycle [23]. UN was proposed as a fuel for fast reactors. Extensive data regarding the irradiation behavior of UN under fast reactor conditions can therefore be found in literature [38,39]. However, data for light water reactors (LWR) is still lacking.

Two key drawbacks have halted the implementation of UN in LWRs. The first one is the neutron absorption of the nitrogen isotope ^{14}N, which constitutes 99.64% of all nitrogen. The nuclear reaction produces ^{14}C and protons during irradiation:

$$^{14}N + n \rightarrow p + {}^{14}C \qquad t_{1/2,^{14}C} = 5700\ a \qquad \sigma_{(n,p)} = 1.83 \pm 0.07\ barn\ [40] \tag{1}$$

^{14}C is a semi long-lived isotope with a half-life of 5700 years [41]. It could be volatilized into the atmosphere in the form of $^{14}CO_2$ or immobilized in the form of carbonates. In any case, this means the creation of undesired additional radioactive waste streams. From a neutronic perspective, the parasitic neutron absorption of the ^{14}N has been estimated to require an increase of ^{235}U enrichment to 4.5 %, compared to 4.2% for UO_2, to compensate for the neutron loss [23]. To resolve this issue, utilization of the less common nitrogen isotope ^{15}N in the synthesis process has been suggested. If 50 or 90% of the nitrogen were to be replaced by ^{15}N,

the ^{235}U enrichment needed to reach the same burn-up would be 3.9 and 3.4%, respectively [23]. Nevertheless, only 0.36% of existing nitrogen can be found as ^{15}N [42], and there are no large scale separation plants for ^{15}N at present. Thus, refinement of ^{15}N would further increase fuel production costs.

The second problem is the tendency of UN powders to oxidize in contact with air, referred to as pyrophoricity. Powders have been observed to self-ignite at temperatures close to 260 °C, producing a mixture of U_3O_8, UO_2, UO_3, U_2N_3, and UN [43–45]. This means that the nitride production must be performed in an inert atmosphere, adding unnecessary complications to the fabrication process. UN is also known for its reaction with water/steam at even lower temperatures, with UO_2 as the main product of the reaction [43,46,47]. This has proved to be the main safety concern related to implementation of UN in LWR systems [48]. Corrosion improvement studies today focus on waterproofing UN to ensure its safe use. It has been reported in literature [49,50] that the use of additives, such as ZrN and AlN, has not shown entirely satisfactory results, and further research is required before any conclusions can be drawn.

3. Theory

3.1. Synthesis of UN

There are different forms of uranium nitrides, depending on the temperature and composition of the solid, as seen in Figure 2. UN, UN_2, and U_2N_3 are the predominant species found in the phase diagram. From the diagram, it is also possible to expect the decomposition of the over stoichiometric nitrides into the mononitride at high temperatures. For simplicity, the term uranium nitride will be used hereafter to describe the mononitride compound. Different methods of UN production and fabrication have been reported thus far, using different uranium sources, such as metallic uranium and uranium oxides, as starting materials [34,51]. Amongst these routes, hydriding-nitriding of metallic uranium [52], carbothermic reduction [53] of uranium oxide, and oxidative ammonolysis of uranium carbides [54] are some examples. This section serves to present and compare the chemistry of some of the routes.

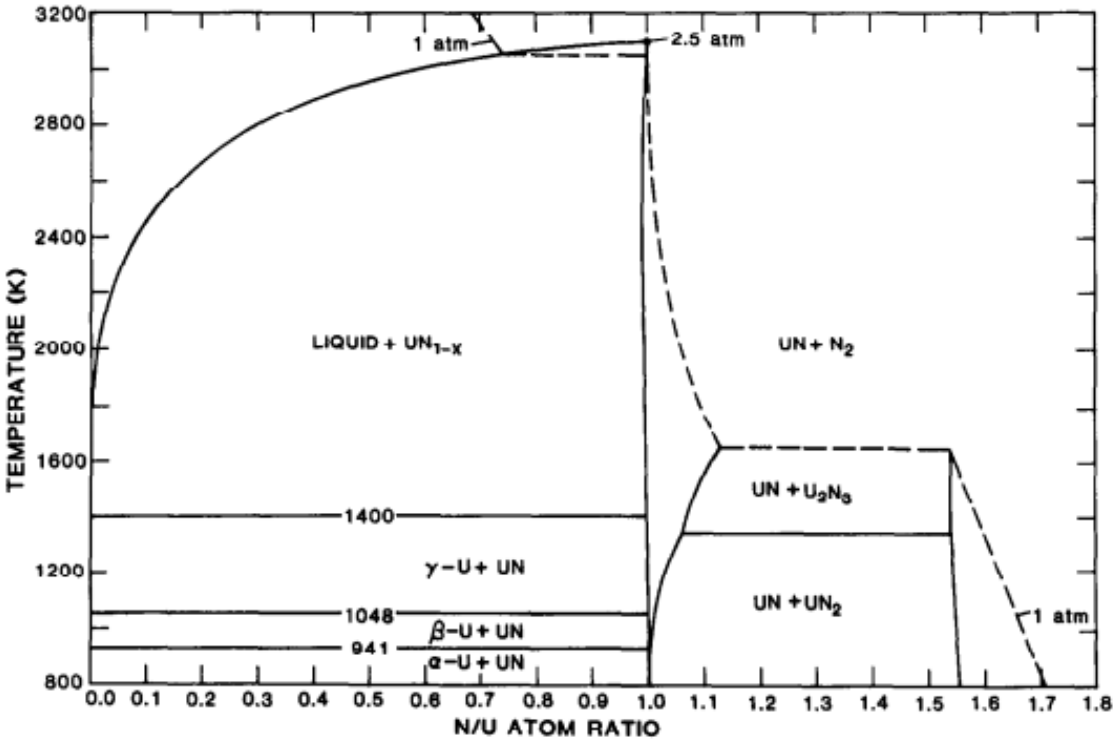

Figure 2. U-N binary phase diagram according to Matthews et al. [39]

3.1.1. Direct nitriding

This technique has the advantage of using uranium metal as a starting material, which is easy to handle and allows the production of high purity UN, with low oxygen and carbon contaminants. Uranium reacts in a nitrogen atmosphere to produce an over stoichiometric nitride as an intermediate product. Afterward, the excess nitrogen is removed by heating under a high purity argon atmosphere or vacuum [34]. The intermediate product has been observed to present a large grain size, which complicates the denitriding process.

$$U\ (s) + N_2(g) \leftrightarrow\ UN_{1.5-1.75}\ (s) \qquad \text{T > 850 °C} \qquad (2)$$

$$UN_{1.5-1.75}\ (s) \leftrightarrow\ UN(s) \qquad \text{900-1300 °C} \qquad (3)$$

3.1.2. Hydriding-nitriding

This process also starts with metallic uranium. It is based on the reaction of uranium with hydrogen to form uranium trihydride, which due to the change in density will be spall off the surface, facilitating the recovery of the hydride in the form of a fine powder, and will expose new metallic surfaces, allowing the reaction to proceed. Temperatures of 200-250 °C are normally required for this reaction to occur [34,51,55–57]. The powder can then be dehydrided to obtain a powder uranium metal. However, the hydride powder can also react readily with N_2 at 300 °C to form uranium sesquinitride. This uranium compound can be decomposed to the mononitride at 1150 °C in an inert atmosphere. This method has the advantage of avoiding carbon and oxygen impurities and has been used in the preparation of other actinide nitrides, such as PuN or ThN [58].

$$2U\ (s) + 3H_2(g) \leftrightarrow\ 2UH_3(g) \qquad \text{200-250 °C} \qquad (4)$$

$$4UH_3\ (s) + 3N_2(g) \leftrightarrow\ 2U_2N_3(s) + 6H_2(g) \qquad \text{300 °C} \qquad (5)$$

$$2U_2N_3(s) \leftrightarrow 4UN(s) +\ N_2(g) \qquad \text{1150 °C} \qquad (6)$$

3.1.3. Carbothermic reduction and nitridation

Carbothermic nitridation is a process that uses UO_2 as the starting material to produce UN. It is based on the reaction of UO_2 with carbon to produce uranium carbide under an inert atmosphere. UC can then be transformed into uranium nitride after reaction under a nitrogen atmosphere (Eq. 8) [56].

$$UO_2(s) + 3C(s) \leftrightarrow\ UC(s) + 2CO(g) \qquad (7)$$

$$2UC(s) + N_2(g)\ \leftrightarrow\ 2UN(s) + 2C(\mathrm{s}) \qquad (8)$$

If uranium dioxide is reacted with carbon under a nitrogen atmosphere, an intermediate uranium carbonitride is observed if temperatures above 1450 °C are used (Eq. 9) [59]. Further reaction with nitrogen can remove the majority of the carbide impurities. Temperatures between 1500 and 1700 °C are commonly used to carry out these reactions (Eq. 9-11) under an H_2/N_2 atmosphere in order to obtain a fairly pure UN [53]. A mixture of H_2/N_2 is used to aid in the reduction of the overstoichiometric UO_{2+x} into UO_2, and to remove the free carbon as HCN, as shown in reaction 12. However, carbon and oxygen are frequently seen as impurities after carbothermic reduction and nitridation. Carbides can cause embrittlement of the Zircaloy claddings [60], therefore, the contaminants contents must be kept as low as possible during the process.

$$UO_2(s) + (2+x)C(s) + \frac{(1-x)}{2}N_2(g) \leftrightarrow UN_{1-x}C_x(s) + 2CO(g) \quad (9)$$

$$UN_{1-x}C_x(s) + \frac{x}{2}N_2(g) \leftrightarrow UN(s) + xC(s) \quad (10)$$

$$UO_2(s) + 2C(s) + \frac{1}{2}N_2(g) \leftrightarrow UN(s) + 2CO(g) \quad (11)$$

$$2C(s) + H_2(s) + N_2(g) \leftrightarrow 2HCN(g) \quad (12)$$

3.1.4. Ammonolysis

A reaction route to produce UN via fluoridation of UO_2 has been investigated to eliminate the carbon contamination and avoid the high temperatures needed in other processes. The UO_2 powder is mixed with ammonium bifluoride (NH_4HF_2) to produce ammonium uranium fluoride [$(NH_4)_4UF_8$]. This reaction is mildly exothermic and can be done at room temperature [61].

$$UO_2\ (s) + 4NH_4HF_2\ (s) \leftrightarrow (NH_4)_4UF_8(s) + 2H_2O\ (l) \quad (13)$$

The subsequent reaction with ammonia gas at 800 °C yields UN_2. Uranium dinitride will decompose into U_2N_3 at 700 °C under an inert argon atmosphere. Afterward, U_2N_3 can be transformed into UN with the same conditions as in reaction 6.

$$(NH_4)_4UF_8(s) + 6NH_3(g) \leftrightarrow UN_2(s) + 8NH_4F(s) + H_2(g) \quad (14)$$

$$UN_2(s) \leftrightarrow \frac{1}{2}U_2N_3(s) + \frac{1}{4}N_2(g) \quad (15)$$

Another route employs uranium tetrafluoride (UF_4), which can be obtained from the UF_6 commonly used today in the first steps of UO_2 fuel production. UF_4 is reacted directly with ammonia at 800 °C to produce uranium dinitride. [61,62] While these processes have several advantages over carbothermic nitridation or direct nitridation, they do not use nitrogen gas as a nitrogen source. Thus, the reactants (ammonium bifluoride or ammonia) would have to be specially synthesized once ^{15}N is taken into consideration to avoid the formation of ^{14}C. [56]

$$UF_4(s) + 2NH_3(g) \leftrightarrow UN_2(s) + 4HF(g) + H_2(g) \quad (16)$$

3.2. Sol-gel process chemistry

Industries today use powder processes for the production of nuclear fuels. However, gelation methods have been developed to provide advantages over powder methods. For example, more homogeneous distribution of elements mixtures can be achieved, and the use of liquid starting

materials, which are simpler to transport and transfer, facilitates remote operation. There are different types of sol-gel methods, such as the external gelation, the ORNL process, and the internal gelation process, each with their own benefits and disadvantages. These processes are based on the precipitation of metal solutions as oxides or hydroxides, usually in the shape of spheres. If the spheres are produced with diameters smaller than 1000 μm, they are known as microspheres. These sol-gel processes have been used in the nuclear industry to produce uranium dioxide [63–65], uranium carbide, and uranium nitride microspheres. Going forward, the last of these will be referred to as uranium microspheres.

In this work, the internal gelation process (IGP) was selected due to previous experiences in our group, leading to a well-established methodology for the production of uranium microspheres. The IGP is based on the hydrolysis and precipitation of metal cations in solution due to the increase in pH when the solution is heated. The starting uranyl nitrate solution is mixed with a complexation agent (urea) and a gelation agent (HMTA) to produce a sol. Temperature is kept low (0 to 5 °C) while mixing to prevent the decomplexation and decomposition of the gelation agent [66]. The sol is then dripped into an immiscible heat-carrying media to start the gelation. The chemistry of the IGP was described by Collins et al. [67] using the following reactions:

$$UO_2^{+2}(aq) + 2[CO(NH_2)_2](aq) \leftrightarrow [UO_2 \cdot 2(CO(NH_2)_2)]^{+2}(aq) \tag{17}$$

$$[UO_2 \cdot 2(CO(NH_2)_2)]^{+2}(aq) + 2H_2O \leftrightarrow UO_2(OH)_2(s) + 2(CO(NH_2)_2)(aq) + 2H^+(aq) \tag{18}$$

$$(CH_2)_6N_4\,(aq) + H^+(aq) \leftrightarrow [(CH_2)_6N_4H]^+(aq) \tag{19}$$

$$[(CH_2)_6N_4H]^+(aq) + 3H^+(aq) + 6H_2O \leftrightarrow 4NH_4{}^+(aq) + 6\,CH_2O(aq) \tag{20}$$

At low temperatures, urea is able to form a complex with the uranyl cation as shown in Eq. 17. Once the temperature increases, the complex is broken, and the cation is hydrolyzed and precipitated as uranyl hydroxide. The HMTA then consumes protons released previously (Eq. 19) and decomposes into ammonium and formaldehyde (Eq. 20). The equilibrium (Eq. 18) is thereby shifted towards the products side by the Le Chatelier's principle.

Vaidya [68] and Collins [67] have also mentioned that hydrolysis of the uranyl ion produces the $UO_2(OH)^{+1}$ monomer (Eq. 21), which has a tendency to form the dimer, trimer, or longer chain polymers. This theory indicates that the precipitation starts with a polymerization.

$$(UO_2)^{2+}(aq) + H_2O \leftrightarrow [(UO_2)(OH)]^{1+}(aq) + H^+(aq) \tag{21}$$

$$n[(UO_2)(OH)]^{1+}(aq) \leftrightarrow [(UO_2)(OH)]_n^{+n}(s) \tag{22}$$

3.3. Pressing and sintering

Pellet pressing is a process for compacting materials, such as powder, granules, or microspheres, in order to form the desired physical shape by reducing the volume and increasing the density of said materials. Nuclear fuel factories, for example, use uniaxial cold pressing to produce the cylindrical pellets used in their fuels. During pressing, the material particles are forced to get close enough to each other that adhesive forces are strong enough to keep them together. The result is a new body with higher density but low mechanical strength, commonly known as "green pellets". When pressing larger aggregates, such as microspheres, the physical integrity of the material might not be conserved after pressing. To achieve even higher density and better mechanical strength, the material must undergo a sintering process. Sintering is based on the densification of materials using high temperatures to remove pores and increase the bonding strength of the particles, resulting in shrinkage of the pellet. [69] The driving force for sintering is the reduction of the surface free energy of the particles. It is facilitated by the movement of atoms through the defects present in the crystalline structure, such as point, line, and planar defects [51].

It was reported in literature that early attempts to sinter uranium nitride pellets proved to be more challenging than the oxides or the carbides. For example, sintering at 1700 °C in vacuum showed no densification of the UN [70], while UO_2 is normally sintered in the range of 1500 to 1800 °C [71,72]. Moreover, increasing the temperature in an inert atmosphere resulted in decomposition of the UN into metallic uranium and nitrogen, which is expected by the phase diagram [73]. The sintering of UN must therefore be performed under a nitrogen atmosphere.

$$UN\ (s) \rightarrow U(l) + \frac{1}{2}N_2(g) \tag{23}$$

It is important, however, to control the nitrogen pressure, as very high pressures resulted in the formation of the undesired compound U_2N_3. On the temperature side, it has been suggested that sintering at 2200 °C for a couple of hours is necessary to achieve densities higher than 90% theoretical density (TD) [74]. The temperature could be lowered to 2000 °C if longer sintering times are used [34].

3.3.1. Spark plasma sintering

Different methods have been used for sintering uranium nitrides. Spark plasma sintering (SPS) is a rather recent technique with similarities to hot pressing sintering. However, the heating is obtained by passing an electrical current through the conducting material, leading to higher heating rates of up to 1000 °C/min [75–77]. Samples are commonly packed in a graphite die, which allows the current to pass through the material being sintered. Simultaneously, pressure is applied to aid in the compaction of the particles inside the die. A schematic representation of the assembly used in these experiments can be seen in Figure 3, where the sample is located between the graphite punchers.

Previous reports have shown that SPS requires lower temperatures and sintering times than more conventional methods to achieve similar densities [76]. Sintering of uranium nitride powders using SPS has been studied before by several authors [38,55,57]. UN pellets with densities of about 90% TD were fabricated by Muta et al. [38] using temperatures as low as

1400 °C. Similar results were observed by Malkki et al. [57]. However, sintering was performed at 1650 °C for only 3 minutes.

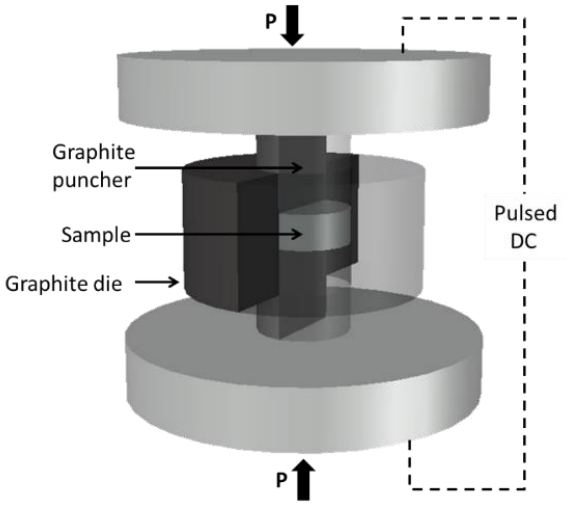

Figure 3. Graphite die representation for SPS, where the pellet is packed. P represents the direction of applied pressure.

3.4. Oxidation and corrosion of UN chemistry

A UN oxidation mechanism was studied and proposed by Dell et al. [43]. Depending on the oxidation environments and thermal conditions different reaction products can be observed, such as UO_2, U_3O_8, and UO_3. In oxygen environments, the reactions start on the surface where the oxygen is chemisorbed. At lower temperatures, about 200 °C, UO_2 is the only observed oxidation product. They also proposed that nitrogen produced in this reaction is released in different ways, it can react with another nitrogen and form nitrogen gas or with UN to form U_2N_3. U_2N_3 is formed as a layer between the UO_2 and UN, and they considered it to be an intermediate product and not a side reaction. Furthermore, they found that the nitrogen gas formed is most likely dispersed in the oxide structure rather than physically trapped in pores, and that it is released only by a diffusion process.

$$UN\ (s) + \frac{2+x}{2}\ O_2(g)\ \rightarrow UO_{2+x}(s) + N \tag{24}$$

$$N + N\ \rightarrow N_2\ (g) \tag{25}$$

$$2UN(s) + N\ \rightarrow U_2N_3(s) \tag{26}$$

$$U_2N_3(s) + 2O_2\ (g) \rightarrow 2UO_2(s) + \frac{3}{2}N_2(g) \tag{27}$$

UO_3 is the observed species once temperatures reach 250 °C. At higher temperatures, U_3O_8 is the final oxidation product obtained in this process. Reactions for the production of higher oxides have been discussed by Rao et al. [78]. They suggest that there can be two nucleation

mechanisms that guide the reaction, and that they are differentiated only by the presence of a separate UO_2 phase in the bulk material. In both cases, the transport of oxygen atoms in a solid material is what causes further oxidation.

UN interaction with water shows a slightly different behavior than with oxygen or air. It is currently known that UN reacts with water to produce only UO_2, as mentioned by Rao et al. [78]. They argue that the lower oxidation potential in addition to the larger size of water molecules compared to oxygen are the reasons for the absence of higher oxide phases, such as UO_3 or U_3O_8, in the hydrolysis products. The water oxidation mechanism was proposed by Dell et al. in 1967 [46]. The reaction between UN and water produces UO_2, with NH_3 and H_2 as gas by-products. Moreover, U_2N_3 was also observed during some of their partial oxidation experiments. Thus, reaction 28 was proposed to occur as a secondary reaction. U_2N_3 can also be further oxidized to UO_2 releasing NH_3 and N_2 as by-products.

$$3\,UN\,(s) + 2\,H_2O \rightarrow UO_2(s) + U_2N_3(s) + 2\,H_2(g) \tag{28}$$

$$UN\,(s) + 2\,H_2O \rightarrow UO_2(s) + NH_3(g) + \frac{1}{2}\,H_2(g) \tag{29}$$

$$U_2N_3(s) + 4\,H_2O \rightarrow 2UO_2(s) + \frac{8}{3}NH_3(g) + \frac{1}{6}\,N_2(g) \tag{30}$$

3.5. Corrosion improvement

Different approaches have been proposed to improve the corrosion resistance of UN to ensure its safe use in LWRs. One of the methods is to reduce the surface area capable of reacting. This can be performed through densification of the material using sintering processes. Another method involves the use of composites, i.e. mixtures of UN with more corrosion-resistant materials, such as UO_2, U_2Si_3, and ThO_2.

Another alternative is to look at the problem from a corrosion perspective. Some elements, such as chromium and aluminum, have been shown to form a stable oxide layer at specific temperature, pressure, and pH conditions that can be used to protect other elements from corroding. This theory has been applied in the corrosion resistance of stainless steels, using chromium to reduce the interaction of iron with air or water. Chromium is known to form a stable chromia scale (Cr_2O_3) at the surface of the steel if the Cr composition in the alloy is higher than 5% [79]. Chromia is stable in a wide range of pH. However, it is been reported that substantial vaporization occurs at temperatures as low as 600 °C [80]. In a PWR reactor, the coolant temperature is maintained between 275 and 315 °C, the dissolved oxygen levels are kept low and the electrochemical potential was measured between -100 and -150 mV [81]. After examination of the Pourbaix diagram in Figure 4, it is possible to conclude that chromia should be stable at reactor conditions, and can therefore be considered a good candidate for UN waterproofing.

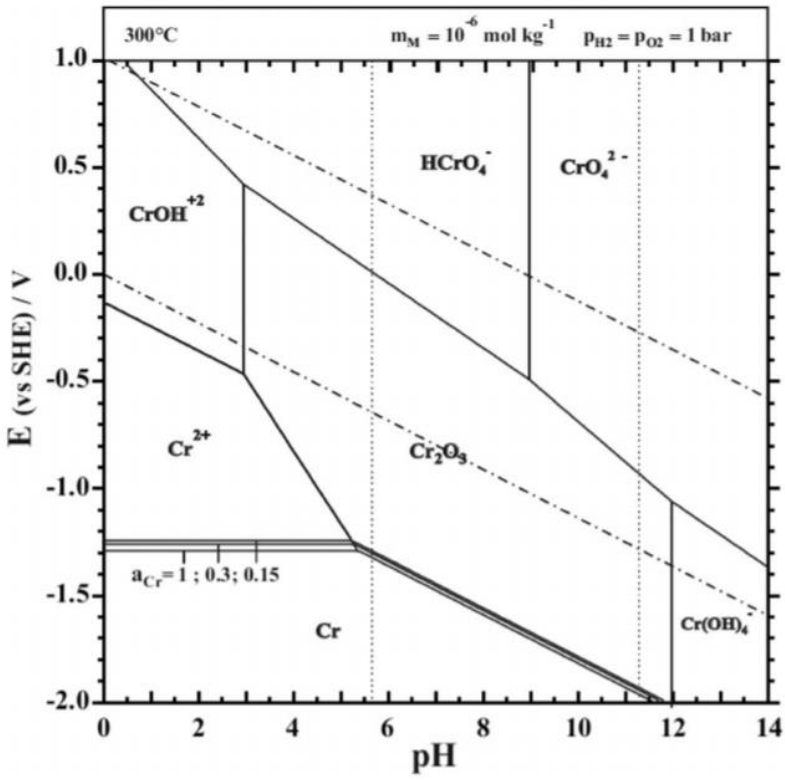

Figure 4. Chromium Pourbaix diagram at 300 °C. The vertical line corresponds to a neutral pH at this temperature [82].

Other additives considered are scale-forming elements such as aluminum, yttrium, titanium, or thorium. The last of these has not been proved to form a protective scale. However, studies have reported that ThN oxidizes faster than UN and that ThO_2 is less soluble in water than UO_2 [83]. Thorium could therefore be investigated as a candidate additive for protection of UN.

The formation of a protective scale is not the only requirement for these additives to be suitable for the nuclear industry. The neutron poisoning induced by the introduction of such additives must be also taken into consideration. The cross-sections for thermal neutron absorption of additive candidates are listed in Table 2. As indicated, yttrium, chromium, and aluminum show the lowest cross-sections, while thorium exhibits one of the highest cross-sections in comparison, 7.37 b. Nonetheless, ^{232}Th can be used as breeding material for ^{233}U, which is a fissile isotope, and could help to balance the neutron losses.

Table 2. Thermal cross-sections of the most abundant isotope of elements candidates for additives and the neutron absorption products.

Additive in its most abundant isotope	**Thermal cross-section (barn)** [42]	**Product(s) after neutron absorption**
^{52}Cr	0.8	^{53}Cr
^{27}Al	0.23	^{28}Al, ^{28}Si
^{89}Y	0.001	^{90}Y, ^{90}Zr
^{56}Fe	2.8	^{57}Fe
^{98}Mo	0.14	^{99}Mo, ^{99}Tc
^{48}Ti	7.9	^{49}Ti
^{232}Th	7.37	^{233}Th, ^{233}U

3.5.1. Solid solutions

In order to achieve a good mixture of the uranium with the additive, a solid solution must be formed. A solid solution is a homogeneous mixture of one element in the crystal structure of the other. There are two types of solid solutions: interstitial and substitutional. As the name suggests, the atomic sites of one component are replaced with the other in a substitutional solution. In an interstitial solution, the atoms of solute are small enough to fit in-between the atoms in the host structure.

Hume-Rothery's work [84] proposes a set of rules which determine whether a solid will be soluble in another. First, the atomic size of the two components should be as similar as possible, and differences greater than 14% are not favorable in the formation of a solution. Second, the electronegativity difference between both elements should be very small. If one element is electropositive and the other electronegative, a compound is more likely to form instead of a solution. Last is the valence factor. A metal of lower valency is more likely to dissolve one of higher valency than vice versa. It has also been mentioned that both compounds should present the same crystal structure in order to form a solid solution.

Table 3. Elemental properties of additive candidates according to Hume-Rothery rules.

Element	**Atomic radius (Å)** [85]	**Atomic radius difference with uranium (%)**	**Electronegativity (Pauling scale)** [85]	**Crystal structure as mononitride (space group)**
Cr	2.06	14	1.66	FCC (NaCl) [86]
Al	1.84	23	1.61	Hexagonal (wurtzite) [87]
Y	2.32	3.7	1.22	FCC (NaCl) [88]
Ti	2.11	12	1.54	FCC (NaCl) [89]
Th	2.45	1.7	1.90	FCC (NaCl) [90]
U	2.41	0	1.83	FCC (NaCl) [91]

Some proposed additives and their properties according to Hume-Rothery's rules are listed in Table 3. As observed, all of them showed the same crystal structure in the nitride form, with the exception of AlN. The atomic radius differences can surpass the 14% limit suggested for aluminum, while chromium is exactly at the limit. Thorium similar atomic properties to uranium, in addition to the existence of a complete solid solution between urania (UO_2) and thoria (ThO_2), indicates that a solid solution is also likely to form for the nitride system.

4. Materials and methods

4.1. Chemicals

The uranium nitrate solutions used as starting materials were produced inhouse by dissolving a metallic bar of natural uranium in concentrated HNO_3 (67%). The precipitated uranyl nitrate crystals were filtered and left to air dry. The final composition of the crystals is uranyl nitrate hexahydrate (UNH) [$UO_2(NO_3)_2 \cdot 6H_2O$]. To prepare the solutions, a known amount of UNH was dissolved in MQ water (18.2 MΩ·cm). Thorium nitrate was received as a solid prepared in-house in the form of $Th(NO_3)_4 \cdot 5H_2O$. Chromium nitrate nonahydrate [$Cr(NO_3)_3 \cdot 9H_2O$] with a purity of 99% was purchased from Sigma Aldrich.

Carbon black (MOGUL-L) provided by the CABOT company was used as the carbon source. Hexamethylenetetramine (HMTA) with 99% purity obtained from Sigma Aldrich was used as the gelation agent. Urea in solid form with 99% purity was obtained from Sigma Aldrich. Laboratory grade Triton X-100 was obtained from Sigma Aldrich and used as a non-ionic surfactant to disperse the carbon powder in the solution [92]. Ultra-pure water (18.2 MΩ·cm) was used for all aqueous dilutions. Silicone oil v-1000 from Rhodorsil was used as the gelation medium. Petroleum ether from Alfa-Aesar was used to wash the oil from the spheres, while NH_4OH solution 28-30% from Sigma-Aldrich was used to wash the unreacted chemicals and to age the spheres.

4.2. Instrumentation

4.2.1. Scanning electron microscopy

Surface analysis of microspheres was performed in a Hitachi TM 3000 tabletop scanning electron microscope (SEM) coupled with an energy-dispersive X-ray (EDX) set in a glove box with $PO_2 < 1$ppm. A Leo Ultra 55 SEM equipped with an EDX detector for chemical analysis was used for SEM analysis of the pellet surface. Both measurements were carried out in high vacuum with a high voltage ranging from 10-30 kV.

4.2.2. X-ray diffraction

X-ray diffraction (XRD) measurements were performed in a BRUKER D2 PHASER XRD which includes monochromatic Cu ($\lambda = 1.54184$ Å) radiation source in a 2θ range of 20˚ - 144˚, and a lynxeye detector. The operating voltage and current used were 30 kV and 10 mA, respectively.

The lattice parameters of the materials can be calculated using the diffractograms. Eq. 31 relates the lattice parameter (a) to the miller index of the crystallographic plane causing the diffraction peak (hkl), the wavelength of the X-rays used (λ), and the interference diffraction angle (θ).

$$a^2 = \frac{(h^2 + k^2 + l^2)\lambda^2}{4sin^2(\theta)} \quad (31)$$

4.1.1. Elemental analysis.

The carbon content in the samples was measured using a LECO CS744 carbon analyzer. Approximately 50 mg of sample was weighed out in an alumina vial and introduced in the machine to be oxidized to CO_2, which is then measured by an infrared detector. Nitrogen and oxygen were measured in a LECO TC-436DR analyzer. Approximately 50 mg of the sample was weighed out in a Sn thin foil boat, closed, and put in a Ni basket. The basket was then introduced in the furnace where it was placed in a graphite crucible and heated to temperatures high enough to melt the samples. Nitrogen is released as N_2 and quantified by measuring the change in thermal conductivity of the He carrier gas. Oxygen reacts with the crucible to form CO_2 which was measured with non-dispersive infrared cells. Measurements in both instruments were done in triplicate to estimate the measurement uncertainties in the instruments.

4.1.2. Thermogravimetric analysis

A thermogravimetric analyzer (TGA) Q-500 from TA Instruments was used for the study of oxidation of samples in air. Samples are placed in an alumina basket held by a Pt wire in the furnace, and the mass change is measured with a precision balance. The thermogravimetric data collected was analyzed using the Universal Analysis software provided by TA Instruments.

4.1.3. Inductively coupled plasma-mass spectrometry

Uranium, thorium, and chromium composition were measured with an inductively coupled plasma-mass spectrometer (ICP-MS) iCAP Q from Thermo Scientific. Samples were dissolved in Aqua Regia (1:3 HNO_3: HCl), filtered, and then diluted with 0.5M HNO3 in the range of calibration (1-50 ppb). An approximate 0.1 ppb detection limit was estimated for the method used.

4.1.4. SPS machine

A modified DrSinter SPS-530ET machine contained within a glovebox under an inert argon atmosphere was used to press and sinter the pellets. The maximum pressure allowed for sintering is 250 MPa and temperatures lower than 2500 °C can be used. Samples were packed into a graphite die with an internal and external diameter of 8 and 20 mm respectively, and a height of 5 cm. A graphite puncher 8mm diameter and 1 cm in length was used to contain the sample and to press it afterward. Graphite paper with a thickness of 0.2 mm was used to prevent the sample from sticking to the graphite die.

4.1.1. Density, superficial area, and porosity.

A gas pycnometer (Accupyc II 1340, Micromeritics) was used to measure the density of the fuel pellets. The instrument works by measuring the amount of helium gas that is displaced after introduction of the material in the chamber. Surface area and open porosity were studied with an ASAP 2020 instrument from Micromeritics, using the BET principle of adsorption and desorption of nitrogen in the pores at low temperatures (-196 °C).

4.1.2. Autoclave

Water and steam interaction tests were performed in a stainless-steel autoclave (Parr Instruments Co., USA), with a reported maximum temperature and pressure of 350 °C and 200 bar, respectively. The autoclave is equipped with a pressure gauge, two gas valves, and a thermocouple, the last of which is connected to a temperature control. A simple representation of the autoclave can be seen in Figure 5. The autoclave was set in a heating mantle, also connected to the temperature control unit. The mantle had no cooling system, thus, only air cooling could be used.

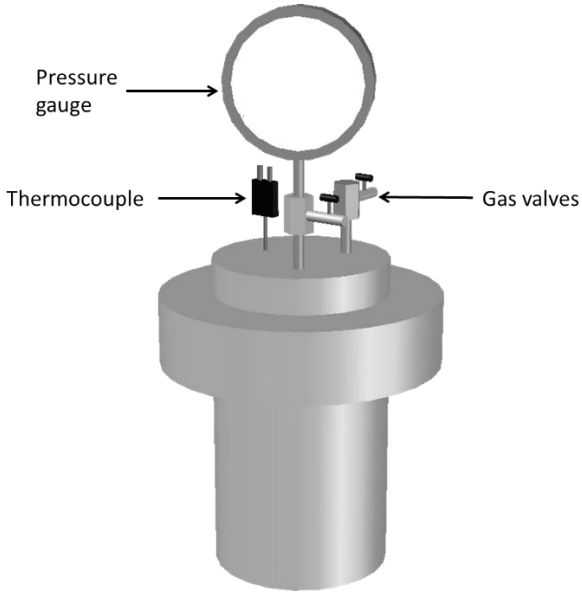

Figure 5. Graphical representation of the stainless-steel autoclave used in the water/steam interaction experiments.

5. Experimental

The methodology followed in this work, presented in Figure 6, was divided into four subgroups: Microsphere preparation (yellow) carbothermic reduction and nitridation (red), pelletization and sintering (grey), and corrosion tests (blue). Each phase will be presented and further described in this chapter.

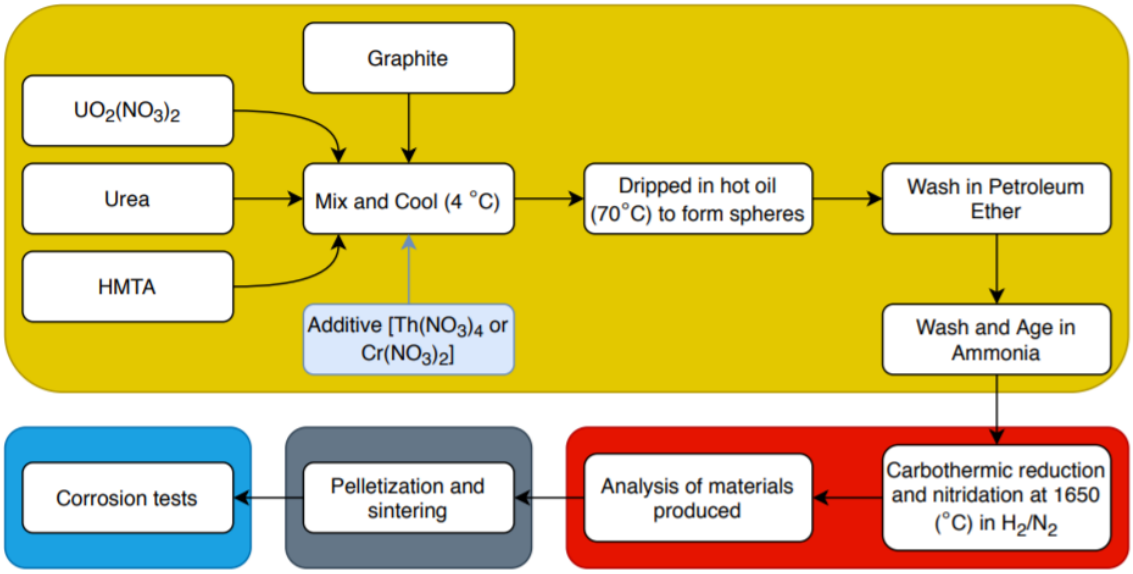

Figure 6. Workflow scheme for the proposed work showing the division of the four main areas: microsphere production, nitride production, pellet manufacturing, and corrosion tests.

5.1. Microsphere production

The internal gelation process was selected for this work due to previous experience with the method in our research group, as well as the other advantages presented previously. The procedure was realized in batches starting with 10 or 15 mL of 1.5 M $UO_2(NO_3)_2$. NO_3^-/UO_2^{2+} ratio was kept at 2 to avoid the use of sub-stoichiometric nitric acid or two sources of uranium. The initial solution was cooled down in a double jacketed beaker connected to a water bath at 4 °C. Metal additives were introduced in this step as needed in molar ratios of 0.05, 0.1, and 0.2 with uranium. Either $Th(NO_3)_4$ or $Cr(NO_3)_3$ were added as solids and left to dissolve under constant stirring. Afterward, urea was added to reach a urea/metal molar ratio of 1.3. The solution was then continuously mixed until complete dissolution. Next, HMTA was slowly added to avoid cluster formation, using a ratio of 1.7 with the metal. Triton X-100 was added as a non-ionic surfactant in a concentration of 0.02 g/milk After homogenization, a carbon source (Carbon Black) was added in a carbon to metal molar ratio of 2.5. The solution was left to mix and homogenize for 10-15 minutes. The ratios used were found experimentally to produce sols which were able to solidify in the oil before reaching the bottom of the column. The final metal concentration in the solution was estimated to be 1.1 M, due to the volumetric expansion through the dissolution of gelation chemicals and carbon.

The solution was transferred and manually dripped into the gelation media (silicon oil) using a plastic pipette, trying to maintain a uniform droplet size. On average, a dropping rate of 0.5

mL/min was used. The microspheres were able to form while falling in the oil as observed in Figure 7. The column used was 30 cm long and 5 cm in diameter. Afterward, the spheres were collected in a sieve, and the remaining silicon oil was removed by washing with petroleum ether for 10 minutes two times. The spheres were also washed in concentrated aqueous ammonia for 10 minutes to remove extra reactants. A final wash with diluted ammonia for 10 minutes was used to age the spheres before letting them air dry for one to two days.

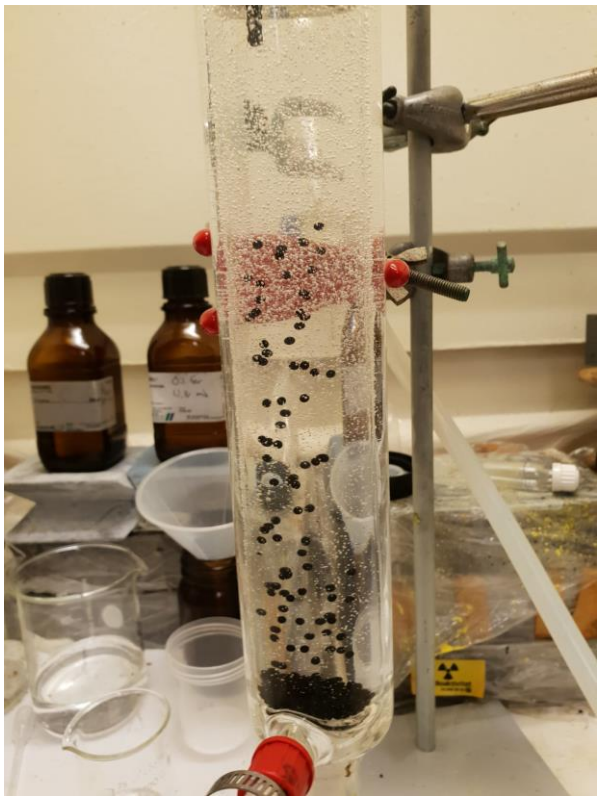

Figure 7. Example of the experimental setup for the internal gelation process, where the forming of the microspheres in the oil column is shown.

5.2. Reduction and Nitridation process

Once the materials were air-dried and analyzed, they were placed in an alumina crucible and taken into an alumina tube furnace (ETF 30-50/18-S) with a maximum operating temperature of 1800 °C. To reduce the cracking of the spheres a 3 °C/min heating rate was used to increase the temperature to 350 °C, where it was kept for one hour to finish the drying process. Afterward, the uranium was reduced to UO_2 and the unreacted organic compounds were reduced to carbon at 800 °C for one hour. The samples were then cooled to room temperature for storage until nitridation. Rates of 10 °C/min were used for heating up to 800 °C and for cooling down. The entire process was performed in a mixed atmosphere gas (5% H_2 and 95% N_2) provided by Air Liquide.

Reduced samples were placed in a clean alumina boat before being introduced in the same furnace used previously. The temperature was raised to 1550 °C at a rate of 10 °C/min where the nitridation was performed for four hours. This was followed by one hour of decarburization at 1650 °C. Afterward, samples were cooled to room temperature at a cooling rate of 10 °C/min.

The temperature profile for the complete process can be seen in Figure 8. Heating and dwelling were performed in a mixed atmosphere gas (5% H_2 and 95% N_2) provided by Air Liquide. The cooling was done in an argon atmosphere. This was important so as to avoid the formation of the undesired U_2N_3 phase after nitridation. Finally, samples were stored in a glovebox with an inert atmosphere and $P_{O2} \leq 1$ppm.

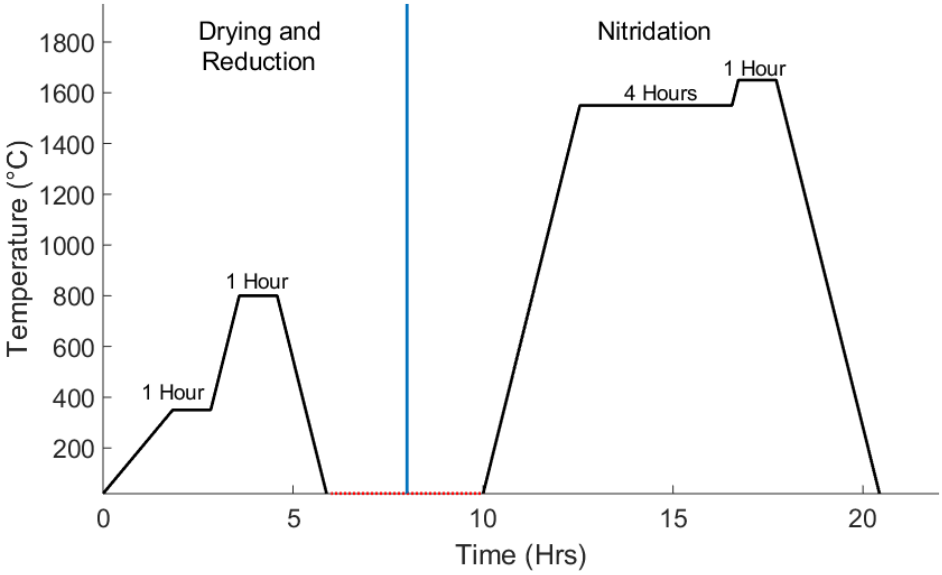

Figure 8. Temperature profile for the carbothermic reduction and nitridation process. Heating and cooling rates of 10 °C/min were used. Heating and dwelling were performed under 5% H_2/N_2 while the cooldown was performed under an inert atmosphere (Argon).

5.3. Pelletization and sintering

Spark plasma sintering was used to manufacture pellets with high density. Sintering was performed under high vacuum (< 10 Pa) to avoid damage to the machine. The temperature was measured with an optical pyrometer, and the pressure was only increased after the temperature reached 400 °C, the lowest value that could be measure with the optical pyrometer. The temperature was raised at a rate of 100 °C/min until it reached the sintering temperature, where it was mainteined for 10 minutes.

Different sintering parameters were studied using the Th doped uranium nitride materials. Thorium composition, temperatures, sintering pressures, and time were modified to observe the effect that they had on the final density of the pellet. A summary of the parameters used during SPS is listed in Table 4. The optimal parameters found for the thorium-doped pellets were used in the manufacture of the (U,Cr)N pellets.

Table 4. Sintering parameters used in SPS for the pelletization of UN and (U,Th)N microspheres. Sintering was performed in high vacuum with a heating rate of 100 °C/min.

Sample name	Thorium molar composition (%)	Sintering temperature (°C)	Sintering pressure (MPa)	Sintering time (min)
UN-1	0	1450	75	10
UN-2	0	1550	75	10
UN-3	0	1650	50	10
UN-4	0	1650	75	5
UN-5	0	1650	75	10
UN-6	0	1650	100	10
UN-7	0	1750	75	10
(U95Th5)N	5	1650	75	10
(U90Th10)N-1	10	1650	75	10
(U90Th10)N-2	10	1750	100	10
(U80Th20)N-1	20	1650	40	10
(U80Th20)N-2	20	1650	75	10

5.4. Density measurements

The density was first estimated knowing the mass and using calipers to measure the height and diameter of the pellets. Afterward, another measurement of the density was obtained using the gas pycnometer mentioned previously in the material and methods section. Due to the difference in density between UN and either CrN or ThN, a direct comparison of materials with different metal ratios is not possible. The percentage of theoretical density was therefore the parameter chosen for comparing the results obtained after sintering. %TD was calculated using the following formula:

$$\%TD = 100 \times \frac{D}{TD} \tag{32}$$

where D is measured density, and TD is theoretical density. To calculate the TD of a material, the crystal structure and composition of the material must be known. As mentioned in Table 3, UN, ThN, and CrN are found in a face-centered cubic (FCC) structure, with corresponding lattice parameters of 4.889 Å [43], 5.160 Å [47], and 4.17 Å [93], respectively. The equation for calculating the theoretical density of FCC materials can be found to be:

$$TD = 4 \times \frac{M_m}{a^3 N_A} \tag{33}$$

where M_m is the molar mass of the compound, a is the lattice parameter and N_A is Avogadro's constant. The lattice parameter of an unknown compound or a solid solution of unknown composition can be found by examining of the diffraction peaks in the X-ray diffractogram.

5.5. Oxidation and corrosion tests

5.5.1. Thermo-gravimetric Analysis

Thermogravimetric analysis was used to study the interaction of the materials produced with oxygen. Samples of approximately 10-20 mg were needed for the analysis. The pellets had to be crushed and small fragments of roughly cubic shape were selected for TGA. The heating ramp used was 5 °C/min up to 900 °C. The furnace was then cooled down to room temperature at a rate of 20 °C/min. A mixture of 90% synthetic air and 10% pure N_2 was used throughout the entire process with a flow of 100 mL/min. Mass change was measured with an accuracy of ± 10 μg.

5.5.2. Autoclave tests

Polished pellets were placed in a stainless-steel sieved basket designed to achieve a larger interface between the pellet and water. 30 mL of ultra-pure water (18.2 MΩ·cm) was used to simulate the coolant in case of fuel cladding failure. Purging with argon was done before the heating process to remove as much oxygen as possible from the autoclave. The temperature was increased and maintained at the desired temperature for two hours. Afterward, the heating was stopped, and the autoclave was left to cool down by air cooling. The autoclave was opened, and the effect of the reaction on the surface of the surviving pellets was studied with SEM. In cases where the pellets did not survive, the water was filtered, using a Whatman® Grade 1 paper filter, to recover the residual powder. In both cases, the pH of the solutions was measured using a PHM240 pH/ION meter from Radiometer coupled with a Radiometer PHC3006-9 electrode filled with a 3M KCl and saturated AgCl electrolyte. The NH_3 concentration was determined through titration with 0.1M HCl.

6. Results and discussion

6.1. Microsphere production and surface analysis

The final product after nitridation was spheres with a dark metallic grey coloration. Diameters between 0.7 and 1 mm were measured for spheres of different batches. The spherical shape was conserved after the heating treatments. However, severe cracking was observed for spheres with high thorium concentration (Figure 9). The cracking could be explained by the use of higher amounts of HMTA needed to precipitate the Th, as Th has a higher oxidation state than the uranyl ion. During the heating process, the unwashed reactants transform into gases, thus causing the cracks observed. Using a higher magnification, the presence of high porosity was observed in all samples. The density of the microspheres was measured and determine to vary between 25 and 50% of their respective theoretical density.

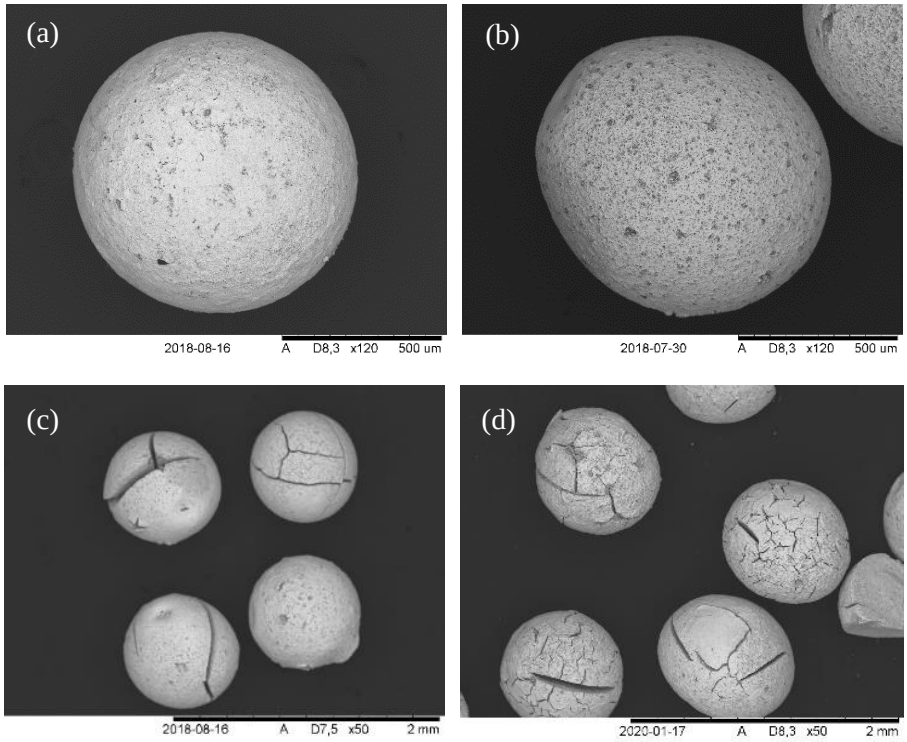

Figure 9. Scanning electron microscopy of uranium nitride and thorium-doped uranium nitride microspheres synthesized using the internal gelation process followed by carbothermic reduction. In order: a) UN, b) (U95Th5)N, c) (U90Th10)N, d) (U80Th20)N.

EDX studies were used to examine the elemental distribution in the surface. It was observed (Figure 10) that all elements (U, Th, C, N, and O) were homogeneously distributed on the spheres. However, EDX signals for Th and U can be misleading, as they are very close in the spectrum. Similarly, C, N, and O signals are close together, and depending on the sensitivity of the machine, overlap could ocurr.

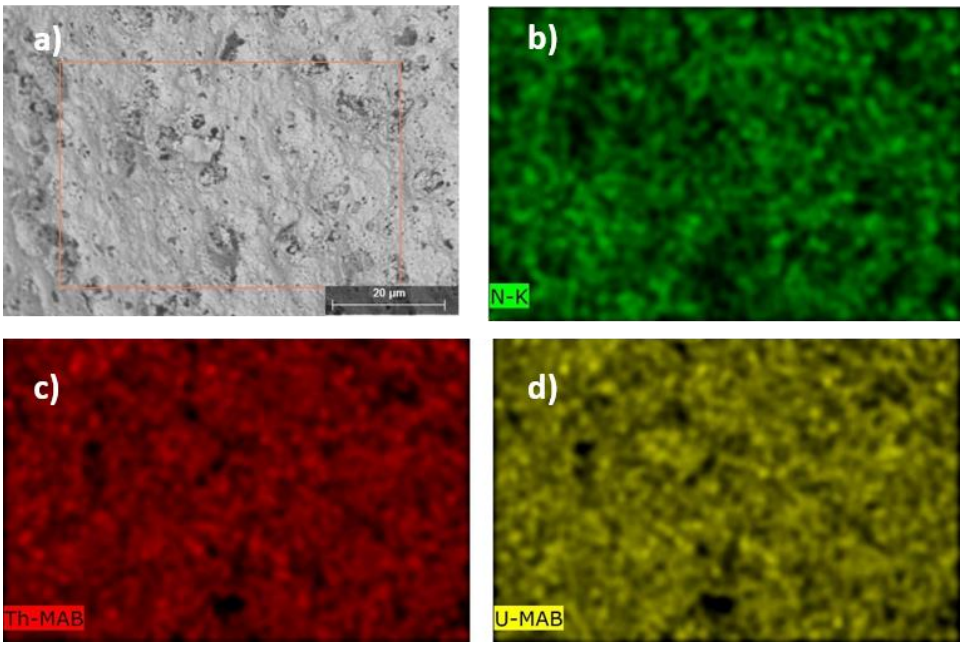

Figure 10. Elemental distribution on the microsphere surface for a (U90Th10)N sample synthesized by carbothermic reduction. In order: a) surface SEM (gray), b) nitrogen (green), c) thorium (red), d) uranium (yellow). Black zones are caused by imperfections on the surface, such as pores.

Chromium seems to disperse in the surface of the spheres at low concentration. However, segregation zones with high chromium content were observed when the Cr ratio was increased. The composition of the spots seems to be either CrN or chromium oxide, However, it was not possible to fully determine it with the resolution of the SEM/EDX. Additionally, severe cracking was also observed for Cr-doped microspheres due to the different behavior of Cr compared to uranyl during gelation.

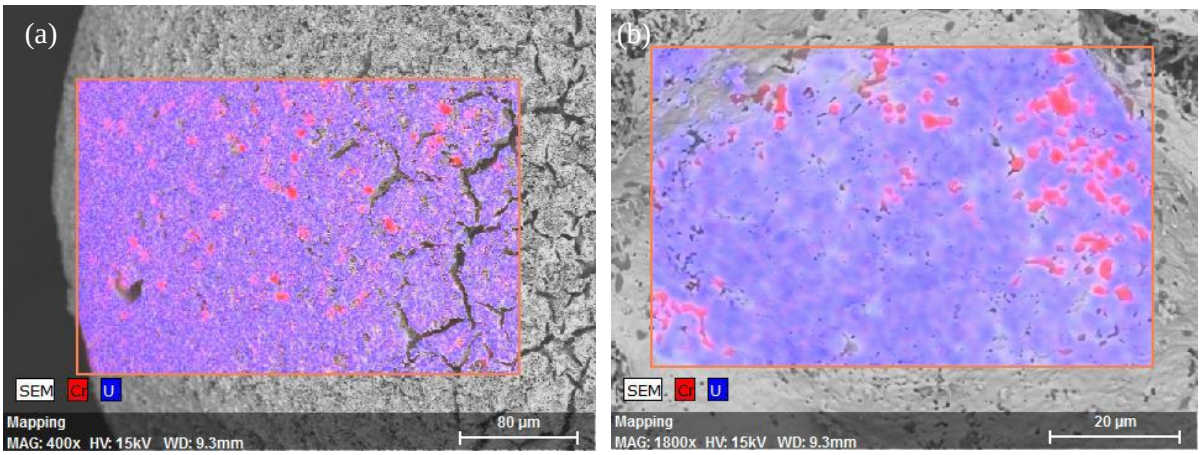

Figure 11. SEM image of an (U80Cr20)N microsphere synthesized through carbothermic reduction showing the chromium (red) and uranium (blue) distribution on the surface.

6.2. Elemental composition and XRD

6.2.1. Th-doped microspheres

One of the main disadvantages of the carbothermic reduction process is carbon and oxygen contamination in the final product. Therefore, the elemental composition of all samples was measured using a carbon and a nitrogen/oxygen analyzers. The measured elemental contents are listed in Table 5. Carbon content ranged between 0.2 and 2.4 wt.-%, while oxygen was found between 0.08 and 0.6 wt.-%. Theoretically, the nitrogen content in a pure UN sample should reach 5.5 wt.-%. However, the maximal nitrogen level was never reached due to the contaminants (C and O). It can be seen that carbon was not completely removed during the decarburization process in some samples (UN-2, UN-4, and UN-6). It is possible that the initial carbon content of these spheres was too high to be removed using the same parameters as with the other materials. Higher temperatures or longer decarburization times may therefore be necessary for these materials. The remaining carbon can be found in two main phases: as a carbide or as graphite. Oxygen is expected to be found in a UO_2 phase remaining after the nitridation process due to incomplete reaction. Additionally, it is possible that some oxidation can occur during transport to the glovebox, increasing the oxygen content of the final product.

Table 5. Elemental composition of thorium-doped uranium nitride microspheres produced through carbothermic reduction. The lattice parameter was estimated using the XRD spectra measured. n.d. stands for not determined. The confidence level for the uncertainties is 2σ.

Sample name	Thorium molar metal fraction (%)	Nitrogen content (wt.-%)	Carbon content (wt.-%)	Oxygen content (wt.-%)	Lattice parameters (Å)
UN-1	0	5.2 ± 0.1	0.27 ± 0.01	0.574 ± 0.002	4.896 ± 0.004
UN-2	0	5.0 ± 0.1	0.6 ± 0.1	0.23 ± 0.02	4.896 ± 0.002
UN-3	0	5.4 ± 0.3	0.011 ± 0.004	0.3 ± 0.2	4.891 ± 0.002
UN-4	0	n.d.	2.0 ± 0.1	n.d.	n.d.
UN-5	0	5.3 ± 0.2	0.2 ± 0.1	0.08 ± 0.02	4.894 ± 0.002
UN-6	0	4.02 ± 0.04	2.3 ± 0.4	0.24 ± 0.06	4.92 ± 0.02
UN-7	0	5.3 ± 0.2	0.01 ± 0.03	0.09 ± 0.02	4.892 ± 0.002
(U95Th5)N	5	5.6 ± 0.4	0.010 ± 0.002	0.26 ± 0.02	4.913 ± 0.006
(U90Th10)N-1	10	4.7 ± 0.8	1.1 ± 0.2	0.3 ± 0.1	4.931 ± 0.004
(U90Th10)N-2	10	5.3 ± 0.4	0.3 ± 0.1	0.4 ± 0.1	4.924 ± 0.002
(U80Th20)N-1	20	5.1 ± 0.1	0.5 ± 0.1	0.6 ± 0.1	n.d.
(U80Th20)N-2	20	3.5 ± 0.2	2.4 ± 0.1	0.37 ± 0.02	4.99 ± 0.01

The presence of the contaminants also affected the diffraction peaks in the XRD. As observed in Figure 12, the peaks were shifted towards lower angles. This change can be explained by the substitution of nitrogen with carbon in the UN crystal structure. Carbide ions are bigger than their nitrogen counterpart, which will stretch the lattice distance between planes. Peaks at smaller angles are therefore expected in accordance with Vegard's law [94]. As no extra visible peaks were observed in the XRD, it is assumed that the carbon in a carbide phase is completely dissolved in the nitride matrix.

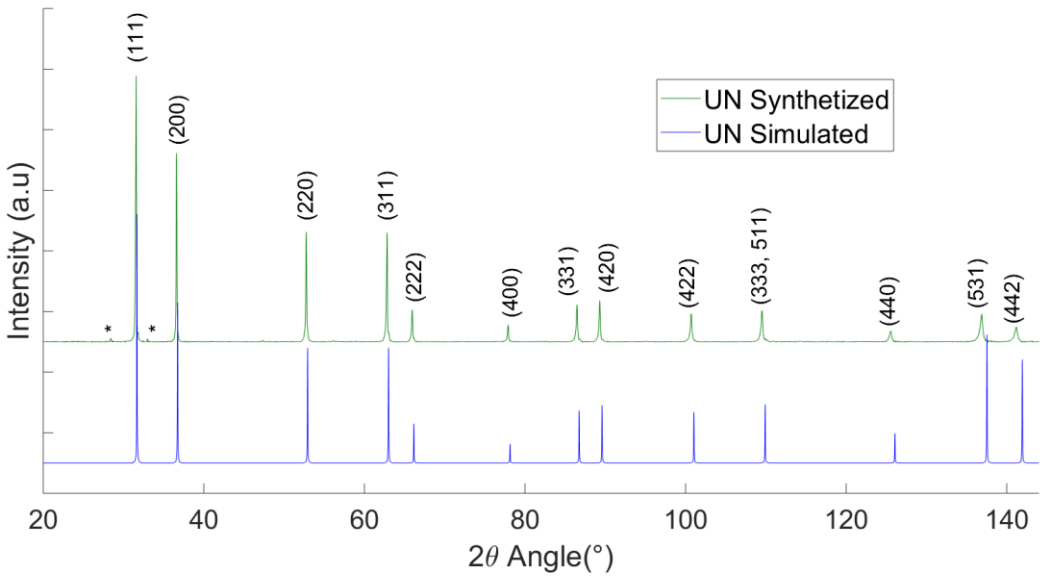

*Figure 12. XRD pattern for a synthetized UN (upper), with an evaluated lattice parameter of 4.894 Å, compared to a simulated XRD pattern for UN (lower), with a lattice parameter of 4.889 Å. * denotes the position of possible UO_2 peaks.*

Similar behavior is observed when thorium is added into the mixture as seen in Figure 13, where the diffraction peaks were also shifted towards lower angles compared to the pure UN. Due to the similarities between uranium and thorium, it is expected that they will form a solid solution when mixed, where thorium atoms will substitute uranium atoms in the crystal structure. The thorium ionic radius is larger than the uranium radius. It will therefore induce the same effect as when carbon replaces nitrogen, increasing the lattice parameter and shifting the diffraction peaks to smaller angles. This effect is more noticeable at larger thorium concentrations in the mixture.

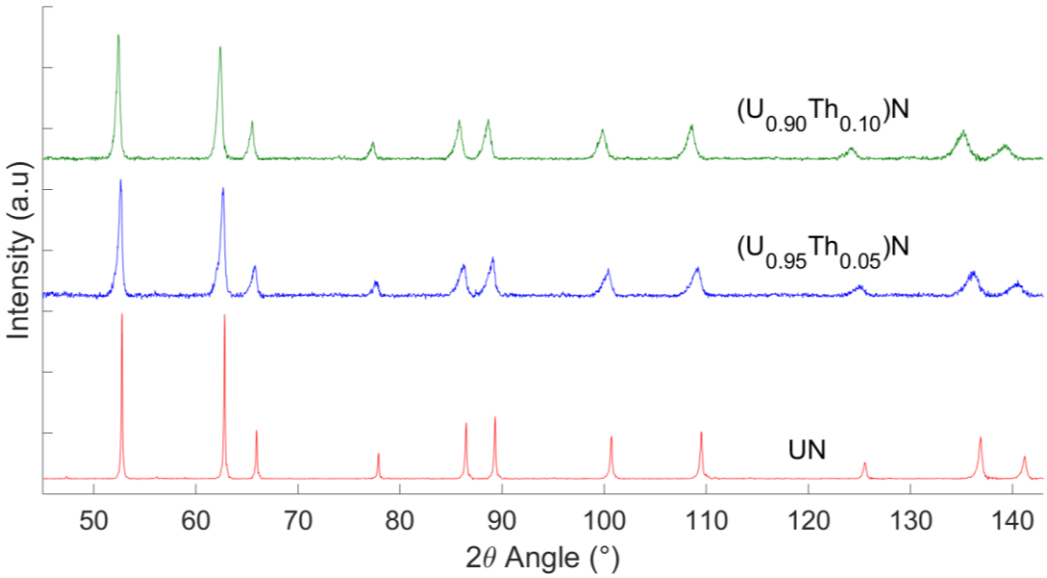

Figure 13. Effect of thorium composition on the XRD pattern for crushed microspheres. From top to bottom: (U90Th10)N with an estimated lattice parameter of 4.924Å, (U95Th5)N with a lattice parameter of 4.913Å and UN with a lattice parameter of 4.894Å.

6.2.2. Chromium-doped microspheres

Chromium-doped materials were a little more challenging to produce. After the nitridation, a pink coloration was observed on the alumina crucibles, which was later attributed to a chromium aluminum oxide phase. It was believed that chromium was being volatilized during the heating process. Its content was therefore measured in all samples at three points during the process: before any heat treatment, after the drying and reduction step, and finally after nitridation. The results are listed in Table 6. As indicated, the chromium contents tend to decrease after each heating step, with the major losses occurring during nitridation. Three cases (marked * in the table) behaved differently, as the Cr content after the reduction step (800 °C) was either the same or higher than the previous step. It is believed that chromium distribution was affected in some spheres more than others after the heating treatments and was therefore not completely homogeneous for the ICP-MS measurements. Several studies [80,95] have been published previously on the loss of chromium at high temperatures in different matrixes. It was reported that at temperatures between 500 and 800 °C, and in the presence of water, Cr forms a chromium oxy-hydroxide compound, CrO(OH), which is a volatile species. However, as aforementioned, the biggest chromium loss was observed during the nitridation process above 1500 °C, where water should be absent. There are two main differences in this step compared to the reduction, i.e. longer reaction times, and higher temperatures. CrN is decomposed into metallic chromium and nitrogen At temperatures higher than 1200 °C, and Cr(g) is suspected to develop and volatilize during the long nitridation treatment [96].

*Table 6. Chromium molar ratio with uranium measured before any heat treatment, after reduction at 800 °C, and after nitridation at 1650 °C. * denotes the samples where the Cr content was higher than in the previous step. n.d. stands for not determined.*

Sample name	Cr mol-% before heating	Cr mol-% after reduction	Cr mol-% after nitridation
U95Cr5 N - 1	5.7	7.7*	1
U95Cr5 N - 2	5.5	5.5*	0.9
U95Cr5 N - 3	12.7	6	2.5
U90Cr10 N - 1	11.2	7	4.11
U90Cr10 N - 2	14.6	9.6	2.5
U90Cr10 N - 3	21.7	19.5	4.9
U80Cr20 N - 1	25.6	18.7	n.d.
U80Cr20 N - 2	31.9	36.3*	6
U80Cr20 N - 3	18.4	11.8	4.6

The elemental composition of the chromium-doped uranium nitride microspheres is listed in Table 7. Carbon content varied in a range similar to that of thorium-doped microspheres, between 0.01 and 1.8 wt.-%. However, higher average carbon contents were measured for Cr-doped microspheres. It is possible that the carbon molar ratio with metals used was higher than necessary for the reaction, or the decarburization time should have been longer, however, this would also further decrease the Cr content. Additionally, larger batches were manufactured for chromium-doped microspheres, which increased the residence time in the hot oil and has been observed to negatively affect the properties of the gelled spheres. Oxygen content was usually

consistent between samples, except for U95Cr5 N - 3, where the carbon content was not enough to remove all of the oxygen.

Table 7. Elemental composition of chromium-doped uranium nitride microspheres produced through carbothermic reduction. The lattice parameter was estimated using the XRD spectra measured. The confidence level for the uncertainties is 2σ.

Sample	Carbon content (wt.-%)	Nitrogen content (wt.-%)	Oxygen content (wt.-%)	Lattice parameter (Å)
U95Cr5 N - 1	1.12	4.390	0.157	4.882
U95Cr5 N - 2	1.21	3.925	0.147	4.883
U95Cr5 N - 3	0.008	5.555	0.543	4.871
U90Cr10 N - 1	0.964	4.315	0.135	4.859
U90Cr10 N - 2	1.71	4.514	0.209	4.871
U90Cr10 N - 3	0.659	4.767	0.167	4.854
U80Cr20 N - 1	1.11	4.650	0.139	4.853
U80Cr20 N - 2	1.80	3.868	0.198	4.846
U80Cr20 N - 3	0.792	4.646	0.227	4.856

X-ray diffractograms of samples with increasing chromium content are presented in Figure 14. Carbon is also present as an impurity, causing an increase in the UN lattice parameter, as with (U,Th)N. Contrarily, chromium is smaller than uranium, which causes a decrease in the lattice parameter, resulting in a peak slightly moved to lower angles. The combination of both effects makes it impossible to determine the composition of a sample using the X-rays diffractogram unless either the Cr or C content is known. It is also important to mention that the absence of any other peaks in the pattern is an indication that other phases are not present, contradicting the observation in the SEM, where a Cr-rich phase was seen to precipitate. However, such phase was very small compared to the UN bulk, and it is possible that there was not enough volume to be measured in the XRD.

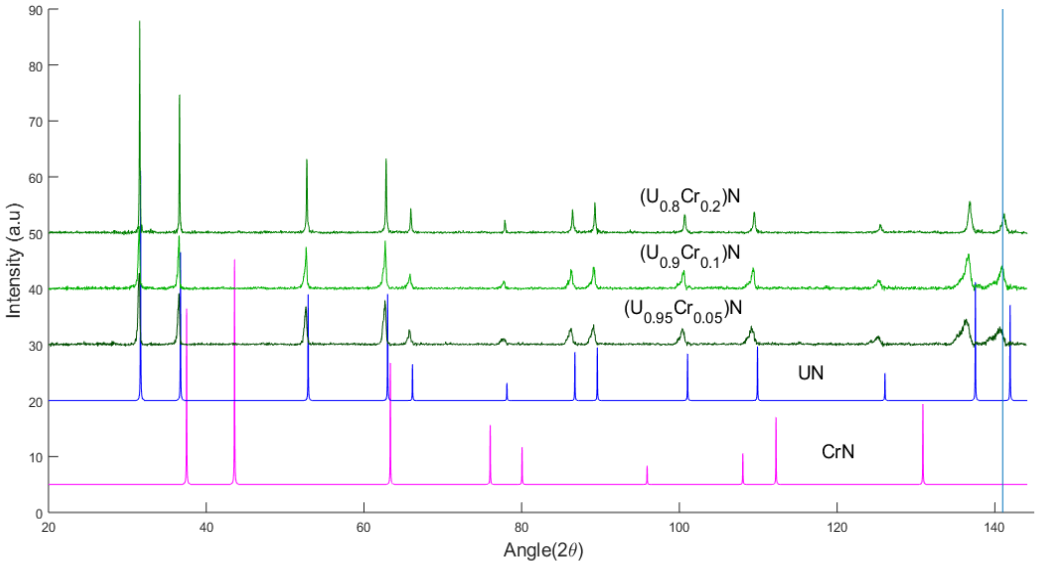

Figure 14. Effect of chromium composition on the XRD pattern for crushed microspheres compared to a simulated XRD pattern for UN with a lattice parameter of 4.889 Å and CrN with a lattice parameter of 4.17 Å. From top to bottom: (U80Cr20)N with an estimated lattice parameter of 4.853 Å, (U90Cr10)N with a lattice parameter of 4.871 Å, and (U95Cr5)N with a lattice parameter of 4.883Å.

6.3. Pellet production and analysis

6.3.1. Pelletization and SPS

From previous experiences, cold pressing of uranium nitride microspheres with conventional sintering has been able to produce pellets with densities up to 80% [50], which does not represent pellets used today as nuclear fuel. For this work, the pellets were manufactured with the aim of increasing the density to values closer to the standard today (≈95%). It has been reported by other authors [38,55] that SPS can press and sinter pure UN powders to produce pellets with densities between 90 and 100% of the theoretical density, depending on the parameters used during sintering. In our case, it was preferable to work directly from microspheres and investigate the difference with powders. A typical heating profile during SPS can be seen in Figure 15. The first shrinkage jump took place when the pressure was increased to the desired value at 400 °C. The red line marks the moment where the sintering process starts, also known as the onset temperature. After this point, the shrinkage increases rapidly as a function of the temperature, until the sintering temperature is reached, and a plateau is observed.

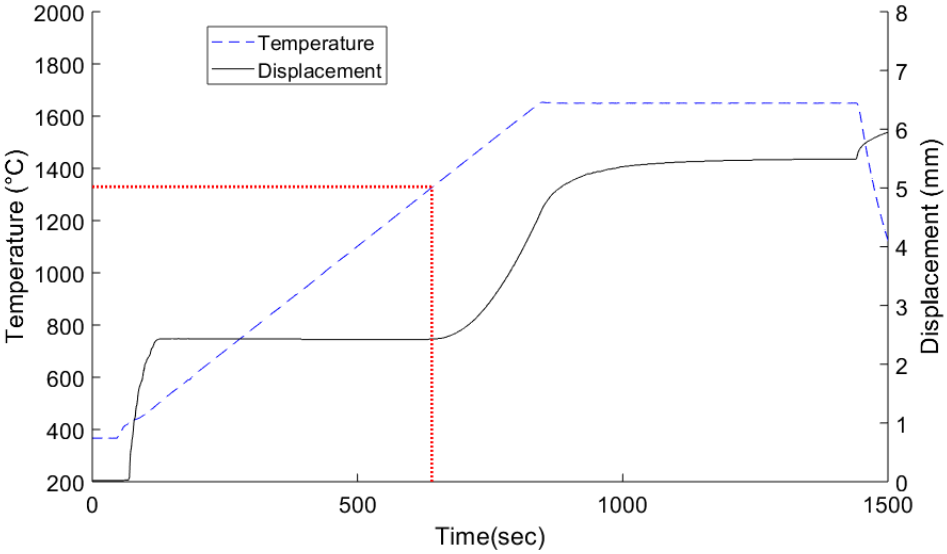

Figure 15. Sintering profile for sample (U80Th20)N-2 showing the temperature profile and the displacement of the punchers. The red line marks the onset temperature found graphically.

After sintering, the graphite die was removed and stored in a glovebox to limit contact with air. Afterward, the graphite paper used to avoid interaction between the UN and the die was removed through grinding with SiC grinding paper. However, the graphite paper was not completely removed, and it could still be observed in the SEM of the pellet surface (Figure 16). The paper seems to be encrusted between the microspheres before the sintering begins, which causes the blackberry structure observed in Figure 16.

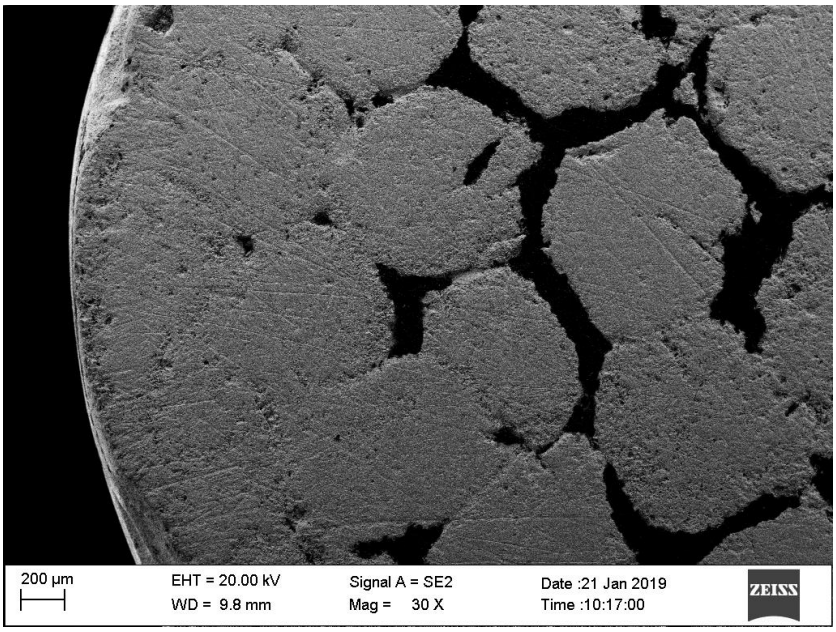

Figure 16. SEM of a Th-doped pellet surface showing the presence of carbon after polishing which marks the shape of the microspheres that could not fuse due to the insertion of graphite paper.

Further polishing was performed using a polishing machine and three different polishing steps: a rough polish using a SiC plate with water as lubricant, a polyester cloth with a diamond suspension (9 µm particles), and for the final step a porous neoprene cloth with a silica suspension (0.25 µm particles). The aforementioned blackberry structure was lost once the

graphite paper was completely removed from the flat sides of the pellets (Figure 17a). The graphite paper could not be completely removed from the edge of the pellets without significantly altering the geometry and can still be seen in the SEM. A high degree of porosity was also observed on the surface of the pellet (Figure 17b). For this particular case, porosity can be explained by the low pressure used in the manufacturing of this pellet (40MPa).

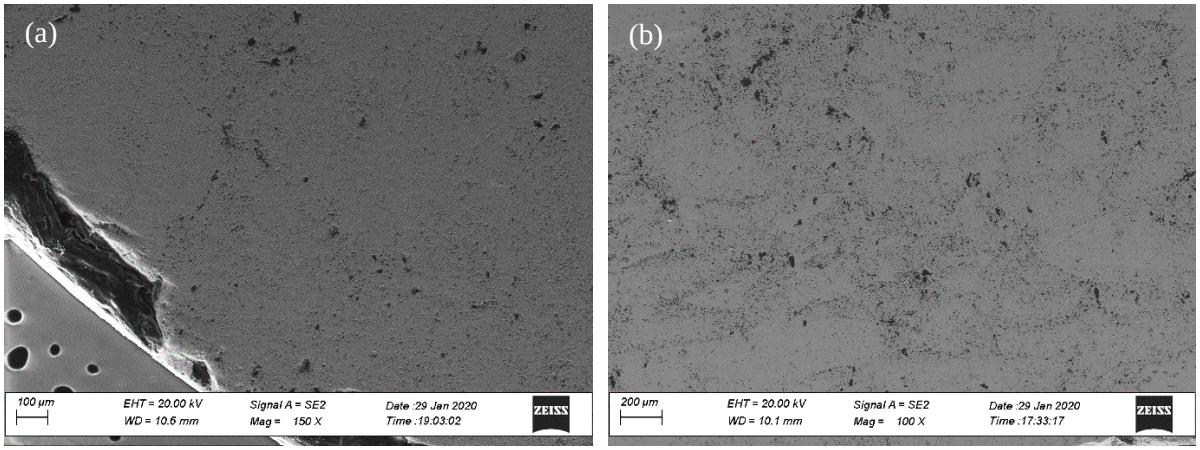

Figure 17. SEM photograph of (a) the surface of the UN-3 pellet and (b) the cross-section of the (U80Th20)N-1 pellet after polishing.

Porosity was observed to be lower in Cr-doped pellets. It is believed that the reason is the parameters used for sintering, which were the best found with the thorium-doped materials. SPS should limit further volatilization of Cr during sintering, as short residence time of the materials at high temperatures is employed. However, as seen in the microspheres, chromium precipitates from the bulk at high temperatures and concentrations. Such precipitates can be more clearly seen in the pellets (Figure 18), where chromium-rich spots are observed, most likely in a metallic chromium phase, as no other elements were identified with the EDX. It is then possible that chromium is precipitating and filling the voids in the solids, which could also explain the slightly higher density of these pellets. Furthermore, the chromium level in the bulk material seems to be nonexistent when measured in the SEM/EDX, suggesting a low solubility of Cr in the uranium nitride phase. This could be expected through comparison with the solubility of chromium in UO_2, which has been reported to be below 0.2 wt-% [97,98].

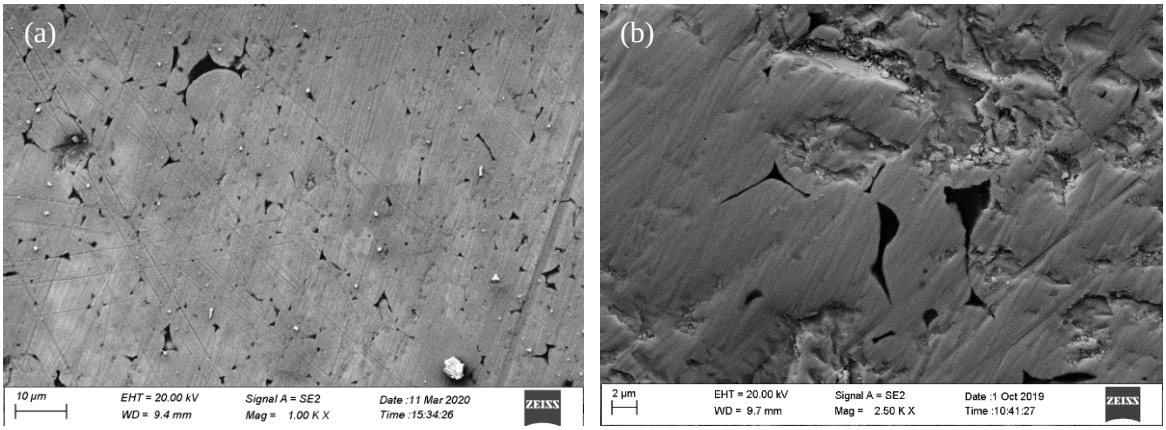

Figure 18. SEM photograph of (a) the surface of the (U80Cr20)N-1 pellet and (b) the surface of the (U80Cr20)N-2a pellet after polishing showing the presence of Cr precipitates through the whole surface.

6.3.2. Density measurements.

Pellet densities were measured after polishing using two different approaches. The first method was to determine the weight and average dimensions of the pellets in order to estimate the density. The second method was to use a gas pycnometer with helium as analyzing gas. From this method an estimation of the density of the material can be calculated. However, it ignores the open pore volume accessible to the gas. A correction must therefore be performed by measuring the open porosity with a BET machine. The results for Th-doped and Cr-doped uranium nitride pellets are listed in Table 8 and Table 9, respectively. Note that the theoretical density was calculated for the impure materials obtained in the carbothermic reduction and nitridation, once the impurities content was known.

Table 8. Comparison of the geometrical and pycnometer densities measured for the undoped and Th-doped uranium nitride pellets. Theoretical densities were calculated using the lattice parameters determined experimentally with the XRD pattern. Pycnometer density was corrected ($\%TD_{Pycn}$) with the open pore volume measurement. The confidence level for the uncertainties is 2 σ.

Sample name	Theoretical density (g/cm^3)	Geometrical density (g/cm^3)	$\%TD_{Geom.}$	Pycnometer density (g/cm^3)	Corrected pycnometer density (g/cm^3)	$\%TD_{Pycn.}$
UN-1	14.26 ± 0.04	11.0 ± 0.2	77 ± 4	13.18 ± 0.06	12.91 ± 0.06	90.5 ± 0.5
UN-2	14.26 ± 0.02	12.9 ± 0.6	90 ± 7	13.51 ± 0.06	13.45 ± 0.06	94.3 ± 0.4
UN-3	14.31 ± 0.02	11.5 ± 0.2	80 ± 5	12.81 ± 0.02	12.72 ± 0.02	88.9 ± 0.2
UN-4	14.32*	12.2 ± 0.8	85 ± 9	13.3 ± 0.1	13.3 ± 0.1	92.5 ± 0.8
UN-5	14.28 ± 0.02	12.7 ± 0.2	89 ± 5	13.36 ± 0.05	13.30 ± 0.05	93.1 ± 0.4
UN-6	14.0 ± 0.2	12.3 ± 0.2	87 ± 5	12.77 ± 0.05	12.67 ± 0.05	90 ± 1
UN-7	14.30 ± 0.02	13 ± 1	91 ± 11	14.07 ± 0.06	14.05 ± 0.06	98.2 ± 0.4
(U95Th5)N	14.10 ± 0.06	12.8 ± 0.4	91 ± 6	13.51 ± 0.06	13.42 ± 0.06	95.2 ± 0.6
(U90Th10)N-1	13.93 ± 0.04	12.4 ± 0.6	89 ± 7	13.15 ± 0.06	13.10 ± 0.06	94.1 ± 0.5
(U90Th10)N-2	13.99 ± 0.02	13.2 ± 0.4	94 ± 6	13.73 ± 0.08	13.66 ± 0.08	97.7 ± 0.6
(U80Th20)N-1	13.79*	10.9 ± 0.2	79 ± 5	12.51 ± 0.03	12.46 ± 0.04	90.4 ± 0.3
(U80Th20)N-2	13.4 ± 0.1	12.1 ± 0.2	90 ± 5	12.80 ± 0.04	12.75 ± 0.04	95.0 ± 0.9

In the case of thorium-doped pellets, densities between 77% and 94% were estimated for the geometrical approach, while the pycnometer densities ranged from 88.9 to 98.2% of TD. The uncertainties of both methods can be used to compare the method precision. As indicated in Table 8, the pycnometer provides uncertainties with one order of magnitude lower than geometrical measurements, indicating a more precise methodology for measuring the density. Corrected pycnometer density results are comparable with values found by other authors [38,55] who used SPS to press pure UN powders instead of UN microspheres. Some work has also been published regarding cold pressing and sintering of uranium nitride microspheres [60,99]. However, the results show that densities did not surpass 85% of TD, even after several hours of sintering.

Large density differences between samples were attributed to the sintering parameters used and will be expanded upon in the next section. It has been noted that the densities measured geometrically are always lower than the pycnometer counterpart. There are two main reasons that could explain such discrepancies: the geometry of the pellets and both open and closed porosity. when calculating geometrical densities, the pellets are assumed to be a perfect cylinder. However, there are always imperfections in the geometry that are created during packing or polishing of the pellets. Moreover, void spaces are not completely removed during sintering, and all of the porosity is taken into consideration in the geometrical measurement. In the gas pycnometer, the geometry is irrelevant as the density is calculated using the volume of gas displaced by the object. Furthermore, the gas molecules permeate the open pores. This volume is thus omitted from the density calculations, and a higher density will be measured. Due to the gas molecules' inability to permeate the closed pores, it is possible to assume that the pycnometer density also provides an estimation of the closed porosity of the pellet. The pycnometer density can be corrected by measuring the volume of open pores, offering a more precise measurement of density that is not affected by the geometry of the pellet. Table 8 shows that density decreased by an average of 0.5%, which is very small when compared to the difference in density due to closed porosity. This implies that the measured open-pore volume represents only a small portion of the total porosity of the pellets.

The sintering parameters used for all chromium samples were identical, and very similar densities can therefore be expected between samples. The density measurements for Cr-doped UN pellets are listed in Table 9. Geometrical densities ranged from 87 to 96%, while the pycnometer density range was slightly higher, between 96 and 100%. These results are comparable to values for Th-doped pellets sintered with the same parameters. Estimated geometrical densities were usually higher compared to Th-doped pellets, most likely due to improved polishing and more symmetrical pellets. The high pycnometer densities measured indicate a very low porosity content, as expected by the sintering parameters used. It can also be noted that the difference between geometrical and pycnometer density is small, which can also be explained by the better geometry of the pellets after polishing.

Table 9. Comparison of the geometrical and pycnometer densities measured for the Cr-doped uranium nitride pellets. Theoretical densities were calculated using the lattice parameters determined experimentally with the XRD pattern. %TD$_{pycn}$ was calculated with the corrected pycnometer density. n.d. stands for not determined.

Sample name	Theoretical density (g/cm^3)	Geometrical density (g/cm^3)	%TD$_{Geom.}$	Pycnometer density (g/cm^3)	Corrected pycnometer density (g/cm^3)	%TD$_{Pycn}$
(U95Cr5)N-1	14.28	13.0	91.1	13.96	13.86	97.05
(U95Cr5)N-2	14.29	13.7	95.6	13.75	13.72	96.02
(U95Cr5)N-3	14.22	12.4	87.3	13.51	13.44	94.52
(U90Cr10)N-1	14.14	13.0	91.6	13.95	13.87	98.05
(U90Cr10)N-2	14.22	13.2	93.0	n.d.	n.d.	n.d.
(U90Cr0)N-3	14.11	13.1	92.6	n.d.	n.d.	n.d.
(U80Cr20)N-1	14.10	13.6	96.4	14.11	14.06	99.69
(U80Cr20)N-2a	14.06	12.7	90.5	n.d.	n.d.	n.d.
(U80Cr20)N-2b	14.06	13.5	95.8	13.80	13.80	98.17
(U80Cr20)N-3	14.12	13.1	92.7	13.95	13.92	98.57

6.3.3. SPS parameters

As previously mentioned, the difference in densities between samples could be explained by the sintering parameters used. The change in temperature demonstrated the greatest effect on density, increasing the density as temperature increased (Figure 19a). The lowest pycnometer density was found to be 92% TD at 1450 °C, while the highest density pellet was manufactured at 1750 °C, where it reached a pycnometer density of 98% TD. As seen in Figure 19b, temperatures of 1550 °C and higher seem to able to eliminate the majority of the open porosity, and significantly reduce the surface area compared to the pellet sintered at 1450 °C.

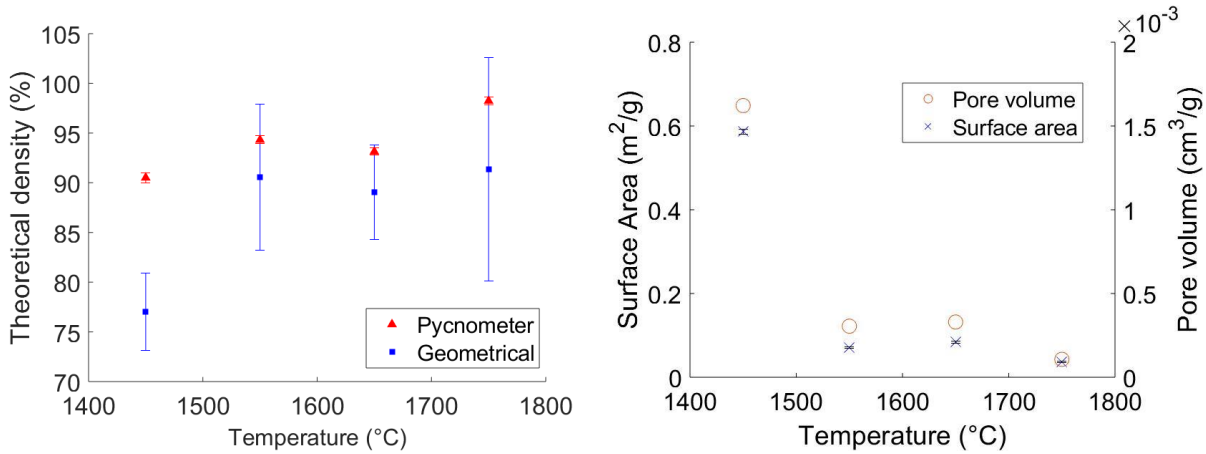

Figure 19. Measured pycnometer (Δ) and geometrical (□) density, surface area (x), and pore volume (○) of UN pellets as a function of the sintering temperature. Sintering pressure and time were maintained constant at 75MPa and 10 minutes respectively. The confidence level for the uncertainties is 2 σ.

The pressure variation showed an effect similar to that of temperature, where higher pressures often produce higher density pellets. These results are further explained in paper 1. Sintering time showed that after 5 minutes at the sintering temperature, the density seemed to reach its maximum value. However, the sintering time was kept at 10 minutes for most U,Th and U,Cr samples for consistency's sake.

6.3.4. Dopant effect in the sintering

During the sintering process, it was observed that there was a slight change in the onset temperature for different materials. As shown in Figure 20, pure UN samples start to sinter below 1000 °C. However, thorium-doped materials show an increase in the onset sintering temperature, and the higher the thorium content, the higher the temperature needed to start the sintering.

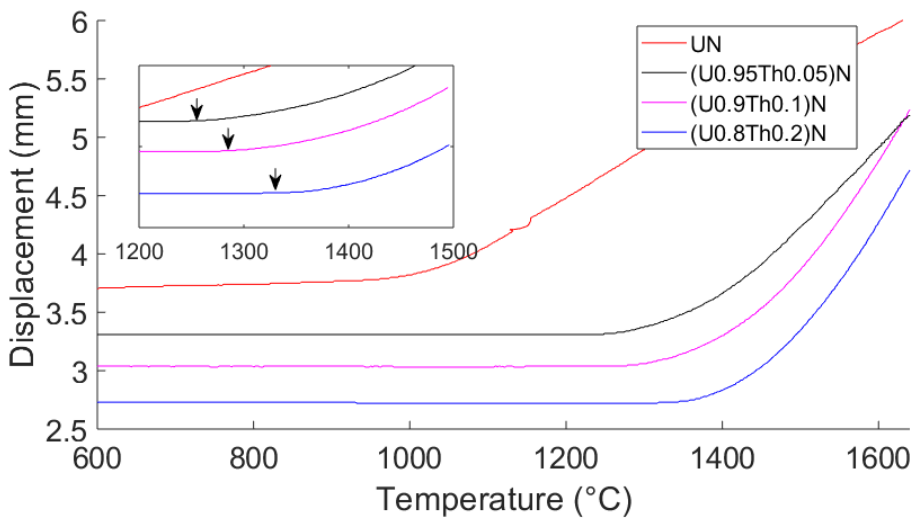

Figure 20. Section of the sintering profile for materials with different levels of thorium doping. Arrows indicate the onset temperature found graphically, showing the temperature where the shrinkage starts.

It is known that higher temperatures are needed to sinter materials with high melting temperatures. However, this does not apply in this case because ThN and UN have similar melting points, 2820 and 2850 °C respectively. To understand the sintering behavior, it was necessary to analyze the crystal organization and what changes occur when thorium is added. The sintering mechanism can be explained by rearrangements and movement of atoms in the crystal structure. Removing defects in the structure, therefore, causes the densification of the materials. Once thorium is introduced in the solid solution, the crystal structure is modified slightly, as observed previously by XRD. The change in the lattice parameter causes an increase in the energy necessary for atoms to move through the lattice, which is then translated into higher temperatures needed for the rearrangement. This theory could explain the increase in the on-set temperature observed in Figure 20. Theoretical studies showed that thorium is most likely to substitute uranium in the structure, causing an increase in the defect migration barrier, and thus, making the interdiffusion harder to achieve. More detailed results on sintering modeling are presented in paper 1.

Similar behavior was seen when chromium was used instead of thorium. However, its effect is not as pronounced as with thorium, and the highest chromium content pellet started to sinter at temperatures below the lowest thorium composition. This can be more easily seen in Figure 21. Theoretical calculations showed that the chromium should decrease the onset sintering temperature if chromium substitutes uranium in the crystal structure, as the lattice distance is shortened, facilitating the interdiffusion of defects in the structure. However, the opposite effect was observed, suggesting that Cr could be dissolved as an interstitial solid solution instead. It is believed that chromium is present as an interstitial solid solution, which could affect the sintering process, but with a less impactful effect.

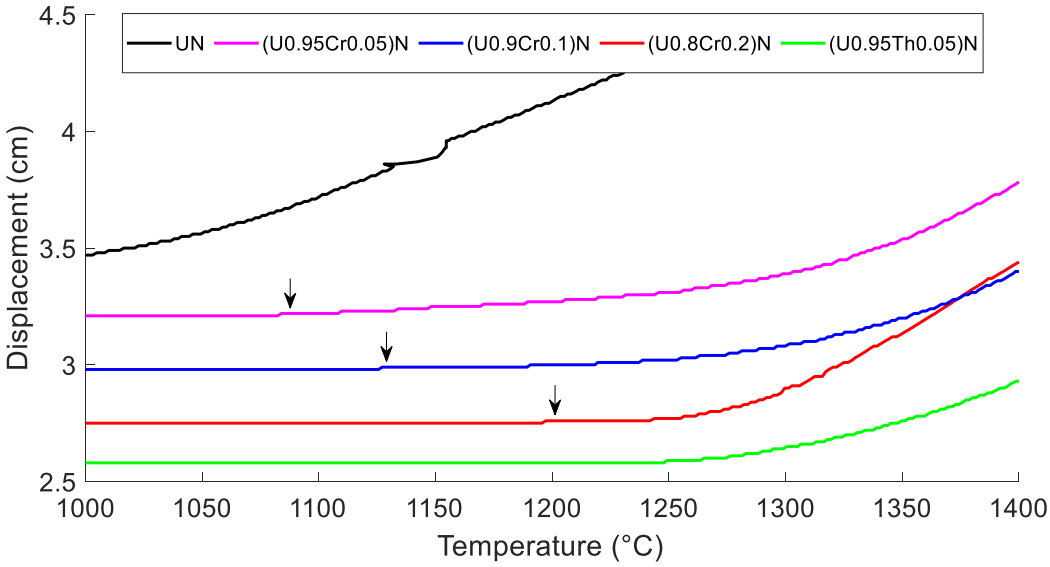

Figure 21. Section of the sintering profile for materials with different levels of chromium doping, compared to low-level Th doping. Arrows indicate the onset temperature found graphically, showing the temperature where the shrinkage starts.

6.4. Corrosion testing

The final objective of this work was to study the corrosion resistance of the materials produced to establish if any improvement was made compared to pure UN. In order to accomplish this, the materials were subjected to two different experiments, oxidation testing in air, and corrosion testing in an environment more similar to a nuclear reactor under normal conditions.

6.4.1. Air oxidation analysis

Thermogravimetric analysis was used to compare the behavior of different Th- and Cr-doped uranium nitride microspheres and pellets in a dried air environment. The average TGA for microspheres with different degrees of Th content can be seen in Figure 22. Triplicates were performed for all samples. However, only one is shown for simplicity's sake. As can be seen, there is a very slow mass gain at low temperatures until the reaction onset point is reached, where the mass change rate increases rapidly. After the maximum weight increase is reached,

the weight tends to decrease instead of being stable, which is attributed by other authors [43,45,100] to nitrogen being released from the pores. For low-density microspheres [(U90Th10)N-2 and UN-1] a reduction process was also observed. This could happen if UO_3 is formed and then reduced to U_3O_8 at higher temperatures, which can be confirmed by the mass increase corresponding to those chemical compounds.

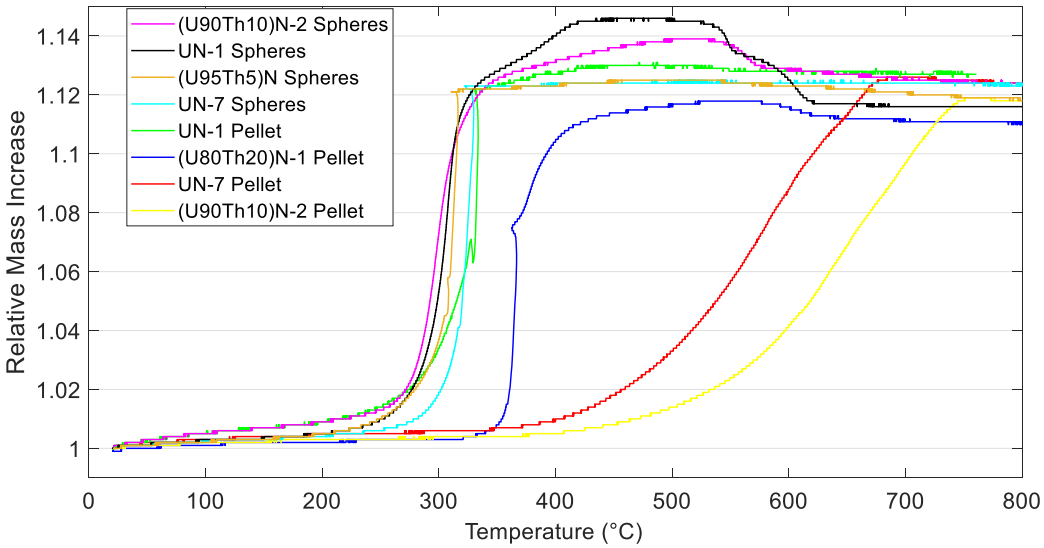

Figure 22. Average TGA for oxidation of uranium nitride and thorium-doped uranium nitride microspheres and pellets using synthetic air.

The onset temperatures and maximum reaction rate temperatures for undoped and Th-doped samples are listed in Table 10. For comparison purposes, the onset temperature was defined as the temperature where the mass change is 5% of the final weight increase. Microspheres showed the lowest reaction onset temperatures, between 125 and 250°C, and maximum reaction rates temperatures between 300 and 325 °C, as can be also seen in Figure 24. Low carbon content and denser microspheres showed a slight increase in both temperatures, which is attributed to a lower surface area accessible to the oxygen to react with the surface. Thorium-doped microspheres exposed to air showed a lower maximum reaction rate temperature and a maximum reaction rate temperature similar to the undoped microspheres. However, the maximum reaction rate was smaller for the doped microspheres, which could suggest that using Th as an additive might slow down the oxidation kinetics in air.

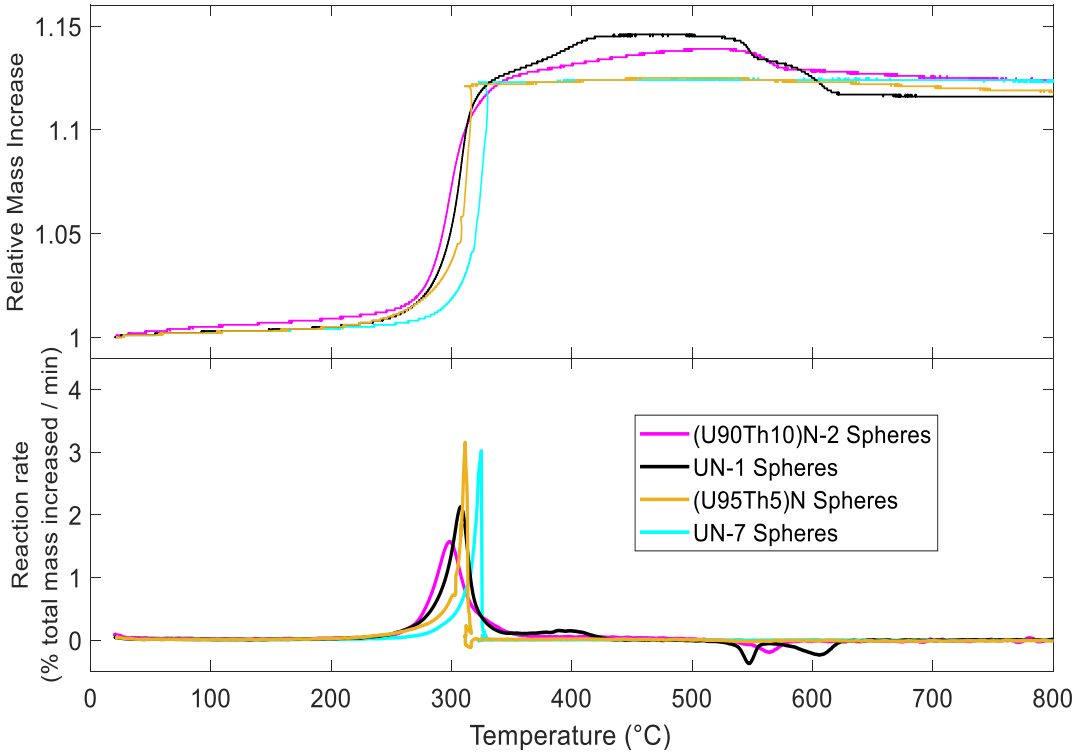

Figure 23. Upper: TGA for oxidation of uranium nitride and thorium-doped uranium nitride microspheres. Lower: Derivative of the TGA used to compare the oxidation rates and to determine the maximum reaction rate temperature

Table 10. Onset and maximum reaction rate temperatures for Th-doped microspheres and pellets with different levels of porosity. The onset temperature was defined as the temperature where 5% of the final mass change was measured. n.d. stands for not determined.

Sample	Total Porosity (% volume)	Onset temperature (°C)	Maximum reaction rate temperature (°C)
UN-1 spheres	71	216	305
(U90Th10)N-2 spheres	n.d.	125	300
(U95Th5)N spheres	66	217	310
UN-7 spheres	58	244	325
UN-1 pellet	9.5	122	330
UN-7 pellet	1.8	315	580-600
(U80Th20)N-1 pellet	9.6	326	360
(U90Th10)N-2 pellet	2.3	416	630-650

Due to the results obtained for microspheres, two sets of pellets were chosen for thermogravimetric analysis, one with high porosity (low density) and one with low porosity (high density). For each set, one sample of pure UN and one with Th doping were selected. TGAs can be seen in Figure 24. It was observed that pellets behaved like microspheres when the porosity was high, with a sudden increase in the reaction rate at temperatures close to 330 °C. This is commonly observed in ignition processes [78]. For low porosity samples, the mass

increase rates were moderated through the process. Therefore, a temperature range for maximum reaction rate was designated instead of a single point. It was found that both onset temperatures and maximum reaction rate temperatures were increased in samples with higher densities and lower porosities. These results are comparable to studies done previously in pellets produced from UN powders instead of microspheres [43,45,78,100]. Moreover, the doping with thorium in the pellets showed a decrease in the oxidation kinetics as both temperatures were higher than their un-doped counterpart. It is believed that substitution of Th in the crystal structure hinders the diffusion of oxygen, and that this effect is observed in pellets due to the lower number of defects after sintering.

The final products of UN and ThN oxidation should be U_3O_8 and ThO_2, respectively. A theoretical mass increase of 11.4% and 7.3% is therefore expected for pure samples. However, all the results showed a final mass increase higher than anticipated. Several reasons could explain these results. It was suspected that it could be a machine calibration error because the endpoint of all UN samples is the same (12.4%), even though they all had different levels of impurities and porosities. A test was performed with a pure UN pellet in an open furnace, where the weight increase was measured to be 10.4%. This is a more feasible result considering the level of impurities in the material. It is also possible that gases were trapped in the close porosities or dissolved in the crystal structure as mention by other authors [45,78], or that a super stoichiometric U_3O_{8+x} was formed instead of U_3O_8.

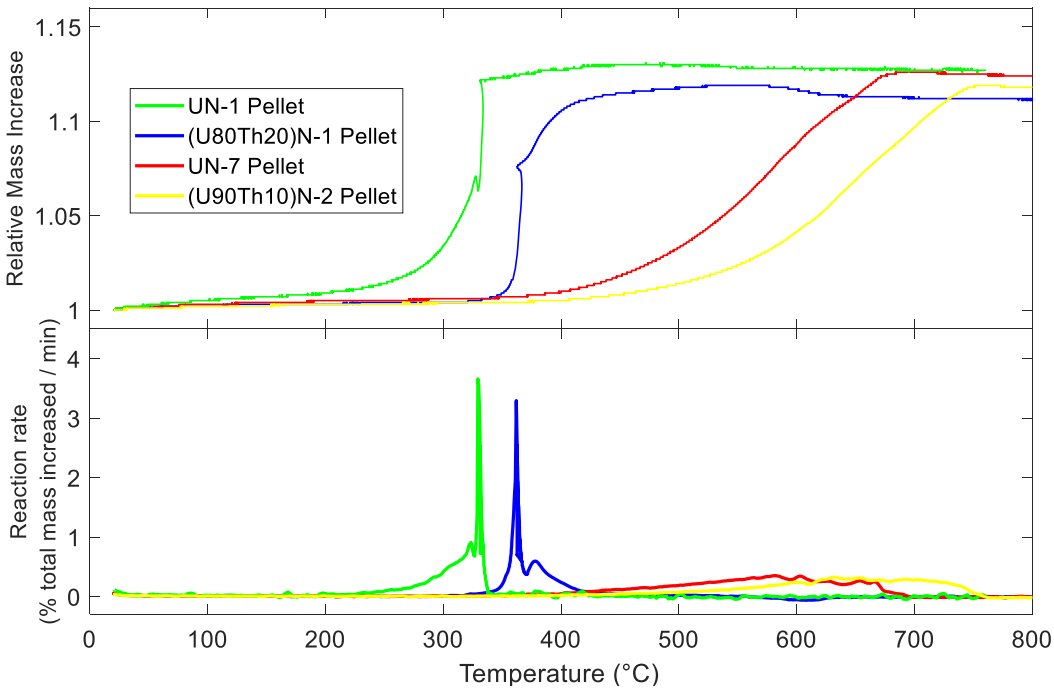

Figure 24. Upper: TGA for oxidation of uranium nitride and thorium-doped uranium nitride pellets showing the difference between pellets with low and high porosity. Lower: derivative of the TGA used to determine the maximum reaction rate temperature.

TGAs for chromium-doped microspheres and pellets can be seen in Figure 25. The addition of chromium seemed to improve the oxidation resistance of UN microspheres by increasing both

the onset temperature and the maximum reaction rate temperature. However, the chromium content was not the defining factor, considering that microspheres with lower Cr content showed higher reaction temperatures. It is then probable, that the high porosity of the microspheres had a greater influence on the oxidation kinetics than chromium doping. Cr-doped pellets showed an oxidation behavior similar to that of Th-doped pellets, where the mass gain rates changed slowly during the treatment, unlike the high reaction rates observed in the microspheres. Furthermore, the biggest reaction delay was observed for pellets with low Cr content where the maximum reaction rate temperature was 660 °C. The pellet with the highest Cr ratio presented a higher onset temperature compared to the undoped UN pellets, 380 vs 315 °C respectively. However, its maximum reaction rate temperature was 610 °C, almost identical to the undoped pellet. These results lead us to believe that the chromium precipitation is somehow accelerating the reaction kinetics, probably due to swelling of the metallic Cr phase after oxidation.

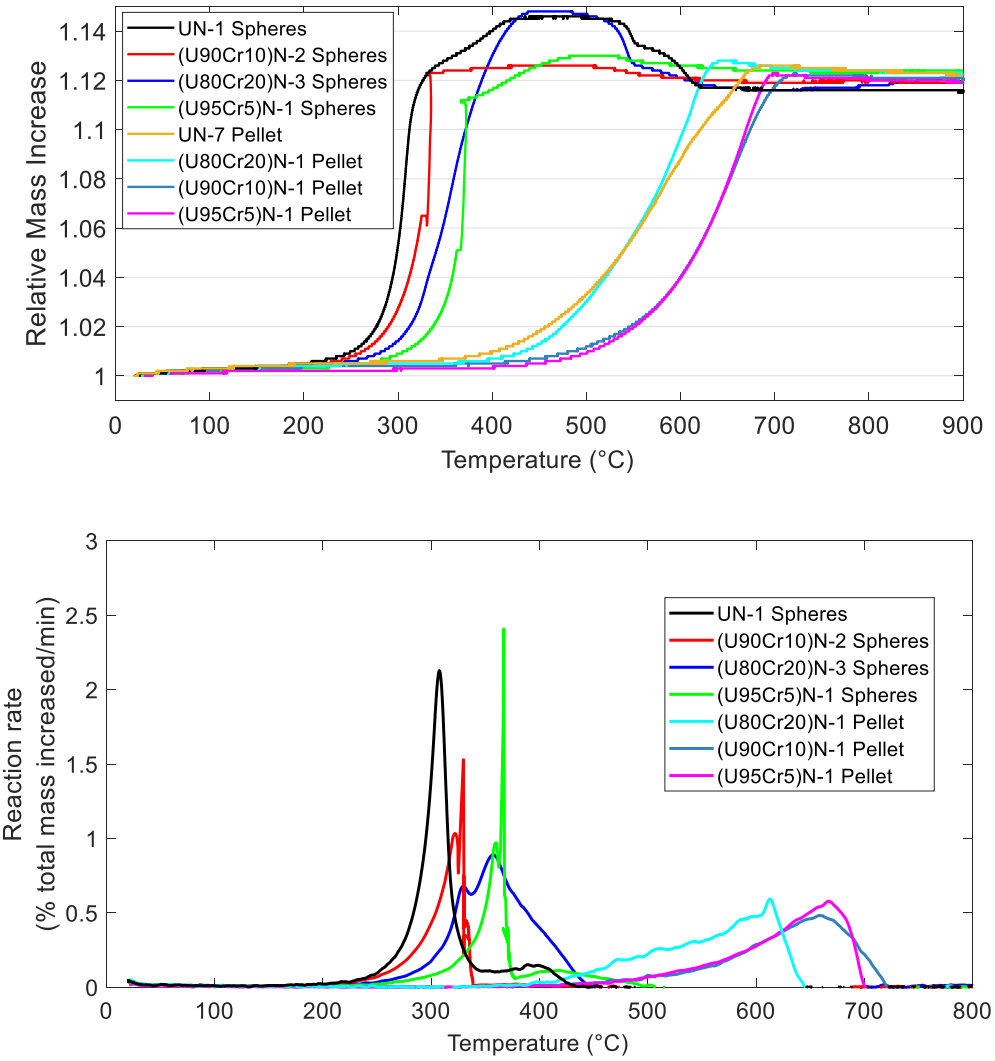

Figure 25. Upper: TGA for oxidation of uranium nitride and chromium-doped uranium nitride microspheres and pellets. Lower: derivative of the TGA used to determine the maximum reaction rate temperature.

Table 11. Onset and maximum reaction rate temperatures for Cr-doped microspheres and pellets with different levels of chromium doping.

Sample	Total porosity (% volume)	Onset temperature (°C)	Maximum reaction rate temperature (°C)
(U95Cr5)N-1 spheres	77	277	365
(U90Cr10)N-2 spheres	73	234	330
(U80Cr20)N-3 spheres	71	250	355
(U95Cr5)N-1 pellet	2.9	464	665
(U90Cr10)N-1 pellet	2.0	426	660
(U80Cr20)N-1 pellet	0.3	380	610

6.4.2. Water/steam corrosion experiments

The results obtained from the air oxidation tests indicate that oxidation resistance was improved in doped materials. Five pellets of (U,Th)N were therefore tested in an autoclave with a water/steam environment to simulate operation conditions of a BWR reactor. Different temperatures were selected to observe any differences in corrosion resistance. A summary of the conditions and results obtained are presented in Table 12. Both UN pellets sintered with SPS were able to withstand at 100 °C and atmospheric pressure with no evident mass change. Surface analysis showed that the oxygen is homogeneously distributed in the edge of the pellet, as seen in Figure 26. These results are a direct improvement compared to previous results from our group in which cold-pressed pellets disintegrated after two hours in boiling water [60].

Table 12. Water/steam corrosion test results. Sample UN-5 was tested in boiling water in air, while the rest of the samples were tested in the autoclave and flushed with argon.

Sample	Maximum temperature (°C)	Pellet disintegration	U conc. (mg/L)	Th conc. (mg/L)	N content in powders (wt.-%)	O content in powders (wt.-%)
UN-5	100 (air)	no	0	-	--	--
UN-2	100	no	0	-	--	--
UN-6	200	yes	1.9	-	0.71 ± 0.04	12.9 ± 0.2
UN-4	300	yes	4.0	-	0.04 ± 0.01	11.59 ± 0.04
(U80Th20) N-2	200	yes	6.6	0.9	0.29 ± 0.01	14.87 ± 0.05

Nonetheless, pellets manufactured with SPS were not able to survive at higher temperatures and turned into a black powder, which was possible to recover and analyze. An unpleasant smell was noticed when the autoclave was opened. This was believed to be ammonia released during the reaction. The pH of the remaining water was measured in these samples, where an increase to alkaline pH was observed and expected due to the dissolution of ammonia. Some uranium and thorium were also measured in the solution, which was unexpected as the solubility of UO_2 and ThO_2 is negligible in water [101]. It is possible that some small particles were not filtered and therefore measured with the ICP-MS.

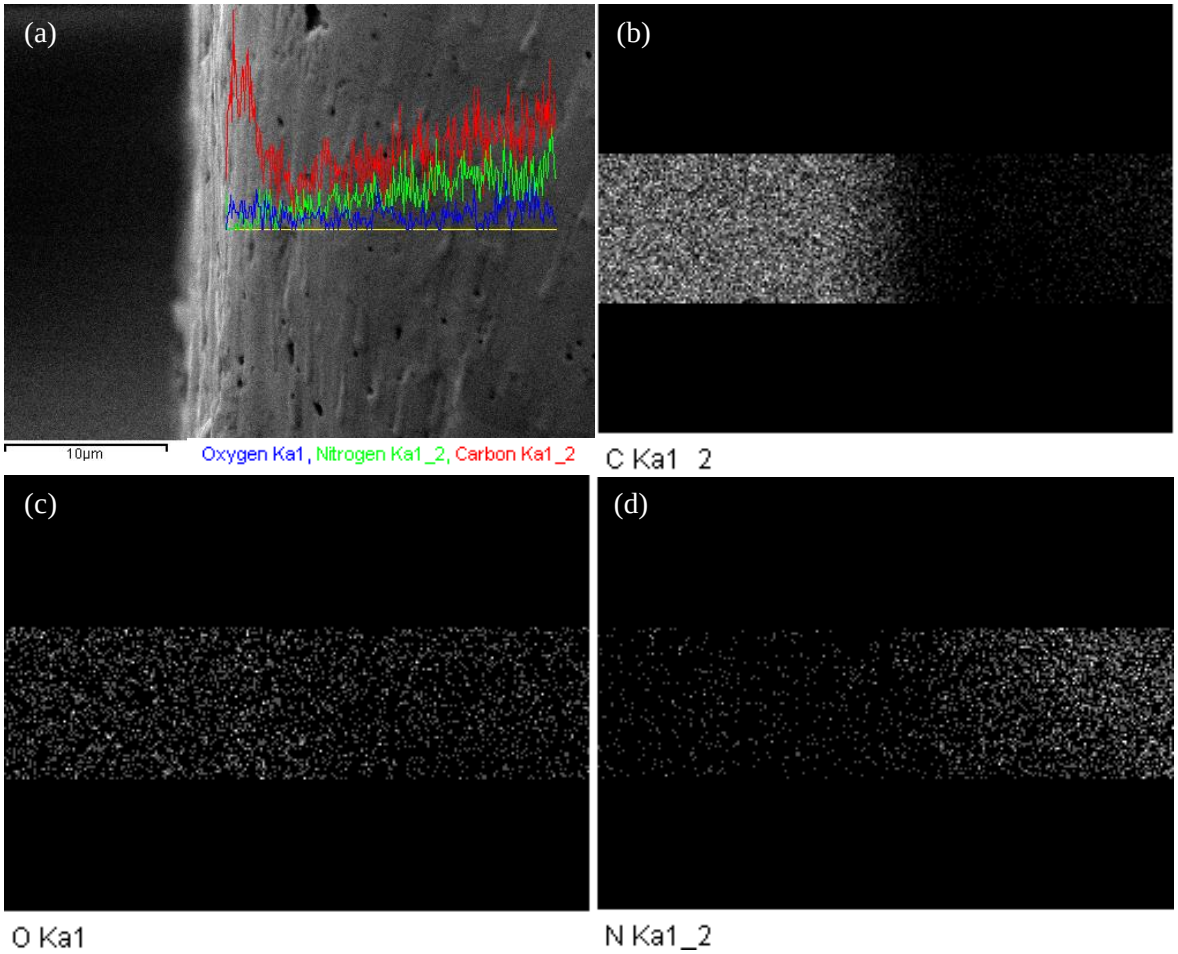

Figure 26. SEM/EDX (a) of the cross-section of the UN-2 pellet after the water interaction test, showing the carbon (b), oxygen (c), and nitrogen (d) distribution in the edge of the surface.

Analysis of the powders showed that some nitrogen remained in the samples after treatment, which has also been reported in previous studies [78,102]. By examining the X-ray diffractograms (Figure 27), it was possible to see that a UN phase was still present in the powders after reaction at 200 °C and 15 bar pressure (UN-6), with UO_2 as the dominating phase. For the Th-doped sample (U80Th20N-2), UN-specific XRD diffraction peaks were observed in addition to the UO_2 and ThO_2. At 300 °C and 85 bar, the sample seems to react completely, as the only product that was observed in the XRD was UO_2. The measured oxygen content was slightly higher than expected for pure UO_2 for some samples, leading us to believe that water was present in the samples. This was later confirmed through TGA analysis.

Thoria formation was corroborated by the powder XRD. However, the expected thoria scale was either not formed or was not stable during the experiment. It is probable that the swelling of the pellet caused the spallation of the scale. These results are, to some extent, discouraging. The thorium doping showed an improvement in the pellet's oxidation behavior in air. However, it was inefficient in the protection of the pellets at the temperature and pressure used, which should be similar to a BWR reactor [103]. Nonetheless, other conditions were not controlled in the autoclave, such as the oxidation potential, which might yield different results, and should be taken into consideration for future studies.

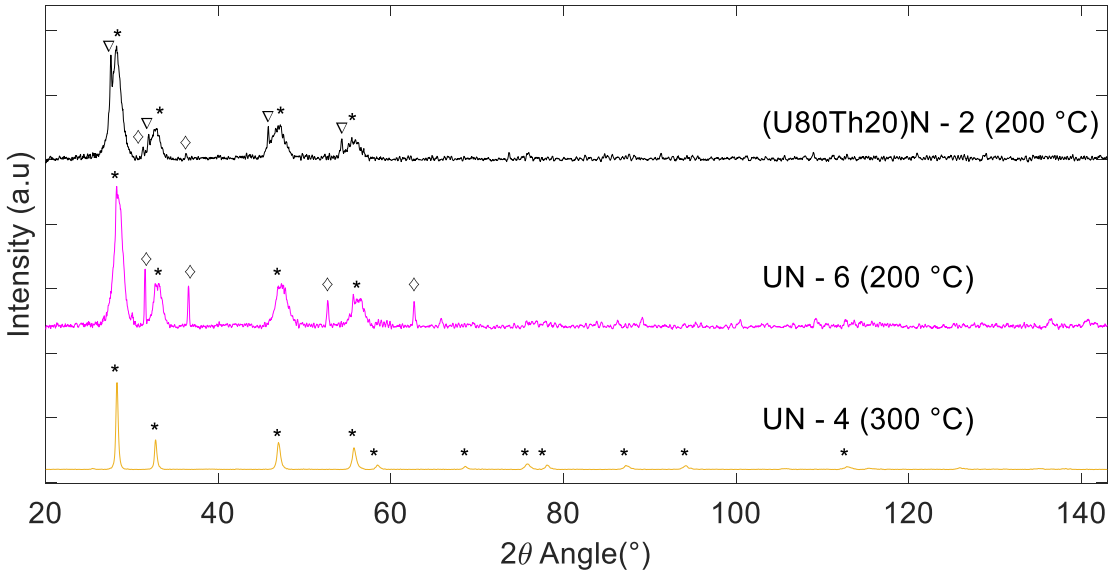

Figure 27. XRD pattern for the collected powders after water testing in the autoclave at different temperatures. The peaks for UN (◊), UO_2 (*), ThO_2 (▽) are marked in the diffractograms.

7. Summary and conclusions

The work done herein was to manufacture pellets of UN fuel doped with either thorium or chromium for possible use as ATFs. The process included the manufacture of UN microspheres, which were pressed and sintered into pellets. In addition, the oxidation resistance behavior towards air and water was investigated after the doped pellets were properly characterized.

It was seen that thorium formed a solid solution with uranium up to 20% thorium molar metal ratio, the highest doping level studied in this work. Cracking of the microspheres was observed after heating treatments, mainly due to the increase in the gelation chemical amounts necessary to precipitate the spheres. Carbon content in the microspheres ranged from 0.2 to 2.4 wt.-%, while oxygen was found between 0.08 and 0.6 wt.-%. These contaminants are common in carbothermic reduction processes and could be explained by short decarburization times.

(U,Th)N microspheres were able to be pressed and sintered into pellets using SPS. Microscopy results showed that the sphere structure was lost during the sintering process. Pellets densities of ~95% TD, which are comparable to densities used today for UO_2, were achieved by sintering at 1650 °C and 75 MPa for 10 minutes.

Exposure of Th-doped UN microspheres to air up to 900 °C showed that the porosity had a more impactful effect on the oxidation kinetics than the thorium doping. However, for sintered pellets, the addition of Th seems to delay the onset of the reaction by approximately 50 °C while reducing the oxidation rates.

UN and (U,Th)N pellets were also exposed to superheated pressurized water. It was observed that UN pellets can survive at 100 °C and 1 bar with no apparent mass change. Interaction at 200 °C and 15 bar showed that UN was hydrolyzed into a UO_2 powder. However, the presence of nitrogen in this powder indicated that the reaction was not completed after two hours. Nonetheless, complete hydrolysis of UN was observed after exposure at 300 °C and 85 bar. Th-doped UN pellets exposed to water at 200 °C and 15 bar showed results very similar to undoped pellets. It was therefore concluded that Th does not seem to offer significant improvements to the corrosion resistance of UN under the conditions of these experiments.

Doping of UN with chromium showed some similarities to thorium doping during microspheres manufacture. Cracking was still present in all microspheres after nitridation. Carbon content varied between 0.01 and 1.8 wt.-%, while oxygen content was usually kept at about 0.15 wt.-%. Unlike with Th-doped UN fuels, chromium doping showed that there is a limit in the solubility of Cr in the UN crystal structure. Precipitation of a chromium-enriched phase was observed in UN microspheres after nitridation. Additionally, it was found that up to 80% of the Cr was volatilized during the heating treatments, which significantly reduced the doping ratios.

As-manufactured (U,Cr)N microspheres were also able to be pressed and sintered using SPS. Surface studies on Cr-doped UN pellets showed the precipitation of metallic chromium in the grain boundaries for highly doped materials. This could explain the slightly higher density (95-98% TD) measured for these pellets compared to (U,Th)N pellets pressed with the same sintering parameters.

Air exposure experiments at high temperatures showed that low chromium doped pellets present somewhat higher onset temperatures (420 °C) and maximum reaction rate temperatures (665 °C) compared to (U,Th)N materials. However, the highest doped (U,Cr)N pellet showed no improvement in oxidation resistance in air, as the same behavior as for an undoped UN was observed.

Both Th and Cr doping showed similar results during air exposure experiments. It is therefore possible to speculate that Cr-doped UN pellets are not going to be able to withstand the exposure to water at 200 or 300 °C. However, further studies must be carried out before any conclusions can be drawn.

ATFs are expected to be less reactive towards air, water, and steam, making the development of an ATF concept a challenge. Results from this study indicate that modifications in the fabrication process of UN pellets can improve the oxidation resistance of UN in air and water. In addition, doping with either Th or Cr reduced the oxidation kinetics of UN pellets and delayed the onset of the reaction in air to higher temperatures. However, if the cladding fails during a reactor normal operation, the fuel could be exposed to superheated pressurized water, and as observed in this work, thorium might not be the ideal doping to protect the UN fuel.

Future work

The aim of this work is to develop and test an ATF concept that can resist oxidation environments at high temperatures. Further testing of Cr pellets in water is necessary to complete the assessment of these elements as a doping material. Additionally, pellet exposure to steam environments at high temperatures could also be investigated.

In case of failure, other elements, such as Al, Y, or Ti, could also be studied to observe whether waterproofing can be achieved. The effect of using a mixture of additives, for example, Cr and Al, could be interesting to investigate.

The coating of UN microspheres or pellets using corrosion-resistant materials, such as Cr_2O_3 or Al_2O_3, could provide interesting results. In addition, the interaction between these two materials should be investigated to determine whether any interdiffusion will occur, which could cause the oxidation of the UN. Moreover, the coating of doped UN pellets with e.g. Cr_2O_3 could slow down the oxidation, allowing the additives to recreate the layer that was not observed in our experiments.

Finally, the interaction of fuels produced with cladding alternatives must also be investigated before it could be implemented for irradiation tests.

Acknowledgments

This work was possible thanks to the Swedish Foundation for Strategic Research (SSF) for funding the SAFETY project (number EM16-0031).

I would like to thank my supervisor Teodora Retegan Vollmer for her support and help during this process; my examiner Christian Ekberg for helping me get started and for being part of my education; and my co-supervisor, Marcus Hedberg, for all the help and things he has taught me since the very beginning (which is more than I could ever expect), as well as his patience to make this work possible.

Thanks to all the members of the SAFETY project which were helpful during the discussions every meeting.

Thanks to all my friends and colleagues in NC/IMR for making this a fun and wonderful journey, especially my office mate Anna for the chatting in the office, and Emma and Gabriele, for the countless hours of boardgames.

And last but not least, thanks to my family and friends everywhere else, who even though they are far away are always supporting me and wishing me the best.

References.

[1] I. Energy Agency, Electricity information: Overview (2020 edition), 2020.

[2] G. Wei, M.T. McCulloch, G. Mortimer, W. Deng, L. Xie, Evidence for ocean acidification in the Great Barrier Reef of Australia, Geochim. Cosmochim. Acta. 73 (2009) 2332–2346. doi:10.1016/j.gca.2009.02.009.

[3] Energy, Electricity and Nuclear Power Estimates for the Period up to 2050, INTERNATIONAL ATOMIC ENERGY AGENCY, Vienna, 2019.

[4] A. Boytsov, An insider's look at uranium production: status, prospects and challenges, 2018.

[5] Aaltonen, I. (ed.), Engström, J., Front, K., Gehör, S., Kosunen, P., Kärki, A., Paananen, M., Paulamäki, S., Mattila, J., Geology of Olkiluoto, 2016.

[6] IAEA., Nuclear Power Reactors in the World., IAEA, 2017.

[7] International Atomic Energy Agency, Protection Against Extreme Earthquakes and Tsunamis in Light of Accident at Fukushima Daiichi Nuclear Power Plant, Vienna, 2012.

[8] K.Y. Spencer, L. Sudderth, R.A. Brito, J.A. Evans, C.S. Hart, A. Hu, A. Jati, K. Stern, S.M. McDeavitt, Sensitivity study for accident tolerant fuels: Property comparisons and behavior simulations in a simplified PWR to enable ATF development and design, Nucl. Eng. Des. 309 (2016) 197–212. doi:10.1016/j.nucengdes.2016.09.009.

[9] S. Bragg-Sitton, Development of advanced accident tolerant fuels for commercial LWRs, Nucl. News. 57 (2014) 83–91.

[10] Nuclear Power Reactors in the World, INTERNATIONAL ATOMIC ENERGY AGENCY, Vienna, 2018.

[11] B.R. Sehgal, Light water reactor safety. A historical review, in: Nucl. Saf. Light Water React., Elsevier Inc., 2012: pp. 1–88. doi:10.1016/B978-0-12-388446-6.00001-0.

[12] Y. Kim, M. Kim, W. Kim, Effect of the Fukushima nuclear disaster on global public acceptance of nuclear energy, Energy Policy. 61 (2013) 822–828. doi:10.1016/j.enpol.2013.06.107.

[13] R. Pöllänen, I. Valkama, H. Toivonen, Transport of radioactive particles from the Chernobyl accident, Atmos. Environ. 31 (1997) 3575–3590. doi:10.1016/S1352-2310(97)00156-8.

[14] S. Hagen, P. Hofmann, LWR fuel rod behavior during severe accidents, Nucl. Eng. Des. 103 (1987) 85–106. doi:10.1016/0029-5493(87)90287-1.

[15] Y. Amano, The Fukushima Daiichi Accident Report by the Director General, Vienna, 2015.

[16] C. Tang, M. Stueber, H.J. Seifert, M. Steinbrueck, Protective coatings on zirconium-based alloys as accident-Tolerant fuel (ATF) claddings, Corros. Rev. 35 (2017) 141–165. doi:10.1515/corrrev-2017-0010.

[17] International Atomic Energy Agency, Accident Tolerant Fuel Concepts for Light

Water Reactors, INTERNATIONAL ATOMIC ENERGY AGENCY, Vienna, 2016.

[18] K.D. Johnson, A.M. Raftery, D.A. Lopes, J. Wallenius, Fabrication and microstructural analysis of UN-U3Si2composites for accident tolerant fuel applications, J. Nucl. Mater. 477 (2016) 18–23. doi:10.1016/j.jnucmat.2016.05.004.

[19] J.C. Brachet, M. Le Saux, M. Le Flem, S. Urvoy, E. Rouesne, T. Guilbert, C. Cobac, F. Lahogue, J. Rousselot, M. Tupin, P. Billaud, C. Hossepied, F. Schuster, F. Lomello, A. Billard, G. Velisa, E. Monsifrot, J. Bischoff, A. Ambard, On-going studies at CEA on chromium coated zirconium based nuclear fuel claddings for enhanced Accident Tolerant LWRs Fuel, in: LWR Fuel Performance/TopFuel/WRFPM, 2015: pp. 31–38.

[20] B.A. Pint, K.A. Terrani, Y. Yamamoto, L.L. Snead, Material Selection for Accident Tolerant Fuel Cladding, Metall. Mater. Trans. E. 2 (2015) 190–196. doi:10.1007/s40553-015-0056-7.

[21] D.J. Park, H.G. Kim, Y. Il Jung, J.H. Park, J.H. Yang, Y.H. Koo, Behavior of an improved Zr fuel cladding with oxidation resistant coating under loss-of-coolant accident conditions, J. Nucl. Mater. 482 (2016) 75–82. doi:10.1016/j.jnucmat.2016.10.021.

[22] R.D. Syarifah, Z. Su ’ud, K. Basar, D. Irwanto, | Sandro, C. Pattipawaej, M. Ilham, Comparison of uranium plutonium nitride (U-Pu-N) and thorium nitride (Th-N) fuel for 500 MWth gas-cooled fast reactor (GFR) long life without refueling, Int J Energy Res. 42 (2018) 214–220. doi:10.1002/er.3923.

[23] G.J. Youinou, R.S. Sen, Impact of Accident-Tolerant Fuels and Claddings on the Overall Fuel Cycle: A Preliminary Systems Analysis, Nucl. Technol. 188 (2014) 123–138. doi:10.13182/NT14-22.

[24] J.M. Harp, P.A. Lessing, R.E. Hoggan, Uranium silicide pellet fabrication by powder metallurgy for accident tolerant fuel evaluation and irradiation, J. Nucl. Mater. 466 (2015) 1–11. doi:10.1016/j.jnucmat.2015.06.027.

[25] G. Vasudevamurthy, T.W. Knight, Production of high-density uranium carbide compacts for use in composite nuclear fuels, Nucl. Technol. 163 (2008) 321–327. doi:10.13182/NT08-A3991.

[26] V.J. Tennery, Godfrey T. G., Potter R. A., Synthesis, characterization, and fabrication of UN, Oak Ridge, Tenn. :, 1970.

[27] H.G. Kim, J.H. Yang, W.J. Kim, Y.H. Koo, Development Status of Accident-tolerant Fuel for Light Water Reactors in Korea, Nucl. Eng. Technol. 48 (2016) 1–15. doi:10.1016/j.net.2015.11.011.

[28] L.H. Ortega, B.J. Blamer, J.A. Evans, S.M. McDeavitt, Development of an accident-tolerant fuel composite from uranium mononitride (UN) and uranium sesquisilicide (U3Si2) with increased uranium loading, J. Nucl. Mater. 471 (2016) 116–121. doi:10.1016/j.jnucmat.2016.01.014.

[29] Y.S. Kim, Uranium Intermetallic Fuels (U–Al, U–Si, U–Mo), Compr. Nucl. Mater. (2012) 391–422. doi:10.1016/B978-0-08-056033-5.00112-9.

[30] R.W. Jones, J.L. Crosthwaite, Atomic Energy of Canada Limited URANIUM CARBIDE FUEL FOR ORGANIC COOLED REACTORS, 1973.

[31] F.B. Litton, The Properties and Irradiation Behaviour of Carbide Fuels: A Literature Survey, Los Alamos, 1968. doi:10.2172/4551282.

[32] S.L. Hayes, J.K. Thomas, K.L. Peddicord, Material property correlations for uranium mononitride: III. Transport properties, J. Nucl. Mater. 171 (1990) 289–299. doi:10.1016/0022-3115(90)90376-X.

[33] J.T. White, A.T. Nelson, J.T. Dunwoody, D.D. Byler, D.J. Safarik, K.J. McClellan, Thermophysical properties of U3Si2 to 1773 K, J. Nucl. Mater. 464 (2015) 275–280. doi:10.1016/J.JNUCMAT.2015.04.031.

[34] K. Johnson, High Performance Fuels for Water-Cooled Reactor Systems, 2016.

[35] D.E. Burkes, G.S. Mickum, D.M. Wachs, Thermophysical Properties of U-10Mo Alloy, 2010.

[36] B. Szpunar, L. Malakkal, S. Chung, M. Mateen Butt, E. Jossou, J.A. Szpunar, Accident tolerant composite nuclear fuels, in: MATEC Web Conf., 2017. doi:10.1051/matecconf/201713003001.

[37] J.T. White, A.T. Nelson, J.T. Dunwoody, D.D. Byler, D.J. Safarik, K.J. Mcclellan, Thermophysical properties of U3Si2 to 1773 K, J. Nucl. Mater. 464 (2015) 275–280. doi:10.1016/j.jnucmat.2015.04.031.

[38] H. Muta, K. Kurosaki, M. Uno, S. Yamanaka, Thermal and mechanical properties of uranium nitride prepared by SPS technique, J. Mater. Sci. 43 (2008) 6429–6434. doi:10.1007/s10853-008-2731-x.

[39] R.B. Matthews, K.M. Chidester, C.W. Hoth, R.E. Mason, R.L. Petty, FABRICATION AND TESTING OF URANIUM NITRIDE FUEL FOR SPACE POWER REACTORS, J. Nucl. Mater. 151 (1988) 334–344.

[40] Y.M. Gledenov, V.I. Salatski, P. V. Sedyshev, The14N(n, p)14C reaction cross section for thermal neutrons, Zeitschrift Für Phys. A Hadron. Nucl. 346 (1993) 307–308. doi:10.1007/BF01292522.

[41] W. Kutschera, The Half-Life of 14 C—Why Is It So Long? , Radiocarbon. 61 (2019) 1135–1142. doi:10.1017/rdc.2019.26.

[42] J. Magill, G. Pfennig, J. Galy, Karlsruher Nuclide Chart, 7th Editio, 2006.

[43] R.M. Dell, V.J. Wheeler, E.J. Mciver, Oxidation of Uranium Mononitride and Uranium Monocarbide*, 1966.

[44] R.M. Dell, V.J. Wheeler, The ignition of uranium mononitride and uranium monocarbide in oxygen, J. Nucl. Mater. 21 (1967) 328–336. doi:10.1016/0022-3115(67)90185-7.

[45] M. Paljević, Z. Despotović, Oxidation of uranium mononitride, J. Nucl. Mater. 57 (1975) 253–257. doi:10.1016/0022-3115(75)90208-1.

[46] R.M. Dell, V.J. Wheeler, N.J. Bridger, Hydrolysis of uranium mononitride, Trans. Faraday Soc. 63 (1967) 1286–1294. doi:10.1039/tf9676301286.

[47] S. Sugihara, S. Imoto, Hydrolysis of Thorium Nitrides and Carbonitrides, J. Nucl. Sci. Technol. 8 (1971) 630–636. doi:10.3327/jnst.8.630.

[48] E.J. Lahoda, F.A. Boylan, F. Boylan, F. Franceschini, S. Johnson, E. Lahoda, J. Secker, P. Xu, C. Back, R. Schleicher, R.G. Cocherell, J. Williams, Development of LWR Fuels with Enhanced Accident Tolerance, 2013.

[49] P. Malkki, The manufacturing of uranium nitride for possible use in light water reactors, Kungliga Tekniska Högskolan KTH, 2015.

[50] A. Herman, C. Ekberg, A Uranium Nitride Doped with Chromium, Nickel or Aluminum as an Accident Tolerant Fuel, 5 (2017). doi:10.4172/2321-6212.1000196.

[51] M. Hedberg, Production and Characterization of ZrN and PuN Materials for Nuclear Fuel Applications, CHALMERS UNIVERSITY OF TECHNOLOGY, 2016.

[52] H. Suwarno, Preparation of Uranium Nitride from Uranium Metal through by Hydriding and Nitriding Process, (2013). doi:10.4028/www.scientific.net/AMR.789.360.

[53] T. Muromura, H. Tagawa, Formation of uranium mononitride by the reaction of uranium dioxide with carbon in ammonia and a mixture of hydrogen and nitrogen— I synthesis of high purity UN, J. Nucl. Mater. 71 (1977) 65–72. doi:10.1016/0022-3115(77)90187-8.

[54] A. Yumi, T. Koji, Preparation of Uranium Carbonitride by Reaction of UC with Ammonia, J. Nucl. Sci. Technol. 5 (1968) 414–418. doi:10.1080/18811248.1968.9732484.

[55] K.D. Johnson, J. Wallenius, M. Jolkkonen, A. Claisse, Spark plasma sintering and porosity studies of uranium nitride, J. Nucl. Mater. 473 (2016) 13–17. doi:10.1016/j.jnucmat.2016.01.037.

[56] B.J. Prewitt, Analysis and implementation of accident tolerant nuclear fuels, Missouri University of Science and Technology, 2017.

[57] P. Malkki, M. Jolkkonen, T. Hollmer, J. Wallenius, Manufacture of fully dense uranium nitride pellets using hydride derived powders with spark plasma sintering, J. Nucl. Mater. 452 (2014) 548–551. doi:10.1016/J.JNUCMAT.2014.06.012.

[58] F. Brown, H.M. Ockenden, G.A. Welch, The preparation and properties of some plutonium compounds. Part II. Plutonium nitride, J. Chem. Soc. 0 (1955) 4196–4201. doi:10.1039/jr9550004196.

[59] S.K. Mukerjee, J.V. Dehadraya, V.N. Vaidya, D.D. Sood, Kinetics of the carbothermic synthesis of uranium mononitride microspheres, J. Nucl. Mater. 185 (1991) 39–49. doi:10.1016/0022-3115(91)90363-C.

[60] A. Sajdova, ACCIDENT-TOLERANT URANIUM NITRIDE, CHALMERS UNIVERSITY OF TECHNOLOGY, 2017.

[61] C.B. Yeamans, G.W.C. Silva, G.S. Cerefice, K.R. Czerwinski, T. Hartmann, A.K. Burrell, A.P. Sattelberger, Oxidative ammonolysis of uranium(IV) fluorides to uranium(VI) nitride, J. Nucl. Mater. 374 (2008) 75–78. doi:10.1016/J.JNUCMAT.2007.06.022.

[62] G.W. Chinthaka Silva, C.B. Yeamans, L. Ma, G.S. Cerefice, K.R. Czerwinski, A.P. Sattelberger, Microscopic Characterization of Uranium Nitrides Synthesized by Oxidative Ammonolysis of Uranium Tetrafluoride, Chem. Mater. 20 (2008) 3076–

3084. doi:10.1021/cm7033646.

[63] A. Deptuła, M. Brykala, M. Rogowski, T. Smolinski, T. Olczak, W. Łada, D. Wawszczak, A. Chmielewski, K.C. Goretta, Fabrication of uranium dioxide microspheres by classic and novel sol-gel processes, in: Mater. Res. Soc. Symp. Proc., Materials Research Society, 2014. doi:10.1557/opl.2014.672.

[64] K. Nagarajan, V.N. Vaidya, Sol-Gel Processes for Nuclear Fuel Fabrication, in: Sol-Gel Process. Conv. Altern. Energy, Springer US, Boston, MA, 2012: pp. 341–373. doi:10.1007/978-1-4614-1957-0_16.

[65] M. Streit, F. Ingold, Nitrides as a nuclear fuel option, J. Eur. Ceram. Soc. 25 (2005) 2687–2692. doi:10.1016/j.jeurceramsoc.2005.03.181.

[66] J. Collins, M. Lloyd, S. Shell, Control of Urania Crystallite Size by HMTA-Urea Reactions in the Internal Gelation Process for Preparing (U, Pu)O2Fuel Kernels, (2005). doi:10.2172/885943.

[67] B.J. L Collins, M.H. Lloyd, The Basic Chemistry Involved in the Internal-Gelation Method of Precipitating Uranium as Determined by pH Measurements*, Radiochim. Acta. 42:3 (1987).

[68] V.N. Vaidya, Status of sol–gel process for nuclear fuels, J. Sol-Gel Sci. Technol. 46 (2008) 369–381. doi:10.1007/s10971-008-1725-0.

[69] D.W. Richerson, Modern Ceramic Engineering: Properties, Processing, and Use in Design, Third edit, Taylor & Francis, 2006.

[70] B.J. Jaques, J. Watkins, J.R. Croteau, G.A. Alanko, B. Tyburska-Püschel, M. Meyer, P. Xu, E.J. Lahoda, D.P. Butt, Synthesis and sintering of UN-UO2fuel composites, J. Nucl. Mater. 466 (2015) 745–754. doi:10.1016/j.jnucmat.2015.06.029.

[71] A.J. Carrea, Sintering of uranium dioxide in an atmosphere of controlled hydrogen content, J. Nucl. Mater. 8 (1963) 275–277. doi:10.1016/0022-3115(63)90048-5.

[72] E.K. Papynov, O.O. Shichalin, A.Y. Mironenko, A. V. Ryakov, I. V. Manakov, P. V. Makhrov, I.Y. Buravlev, I.G. Tananaev, V.A. Avramenko, V.I. Sergienko, Synthesis of High-Density Pellets of Uranium Dioxide by Spark Plasma Sintering in Dies of Different Types, Radiochemistry. 60 (2018) 362–370. doi:10.1134/S1066362218040045.

[73] V.J. TENNERY, T.G. GODFREY, R.A. POTTER, Sintering of UN as a Function of Temperature and N2 Pressure, J. Am. Ceram. Soc. 54 (1971) 327–331. doi:10.1111/j.1151-2916.1971.tb12306.x.

[74] F. Goldner, Development strategy for advanced LWR fuels with enhanced accident tolerance, Present. to Enhanc. Accid. Toler. LWR Fuels Natl. Metrics Work. Oct. (2012) l5.

[75] M. Omori, Sintering, consolidation, reaction and crystal growth by the spark plasma system (SPS), Mater. Sci. Eng. A. 287 (2000) 183–188. doi:10.1016/S0921-5093(00)00773-5.

[76] S.H. Risbud, C.-H. Shan, Fast consolidation of ceramic powders, Mater. Sci. Eng. A. 204 (1995) 146–151. doi:10.1016/0921-5093(95)09951-4.

[77] M. Eriksson, Z. Shen, G. Svensson, Policy document for National Spark Plasma Sintering (SPS) Facility About SPS Access, 2018.

[78] G.A.R. Rao, S.K. Mukerjee, V.N. Vaidya, V. Venugopal, D.D. Sood, Oxidation and hydrolysis kinetic studies on UN, J. Nucl. Mater. 185 (1991) 231–241. doi:10.1016/0022-3115(91)90340-D.

[79] K.G. Field, M.A. Snead, Y. Yamamoto, K.A. Terrani, Handbook on the Material Properties of FeCrAl Alloys for Nuclear Power Production Applications, 2017.

[80] H. Falk-Windisch, J.E. Svensson, J. Froitzheim, The effect of temperature on chromium vaporization and oxide scale growth on interconnect steels for Solid Oxide Fuel Cells, J. Power Sources. 287 (2015) 25–35. doi:10.1016/j.jpowsour.2015.04.040.

[81] P. Aaltonen, H. Hanninen, WATER CHEMISTRY AND BEHAVIOUR OF MATERIALS IN PWRs AND BWRs, (n.d.).

[82] Potential-pH Diagrams for Ni-Cr-Fe Alloys and Pb Adsorption on Ni-Cr-Fe Alloys Surfaces in Water at 25°C and High Temperature (250-350°C), (2018). doi:10.1149/2.1291807jes.

[83] G. Heisbourg, S. Hubert, N. Dacheux, J. Purans, Kinetic and thermodynamic studies of the dissolution of thoria-urania solid solutions, J. Nucl. Mater. 335 (2004) 5–13. doi:10.1016/j.jnucmat.2004.05.017.

[84] U. Mizutani, Hume-Rothery Rules for Structurally Complex Alloy Phases:, CRC Press Inc, 2016.

[85] J.R. Rumble, Properties of the elements and inorganic compounds, in: CRC Handb. Chem. Phys., CRC Press/Taylor & Francis, Boca Raton, 2018: p. Internet Version.

[86] L. Zhou, D. Holec, M. Bartosik, F. Körmann, B. Grabowski, J. Neugebauer, P. Mayrhofer, Structural stability and thermodynamics of CrN magnetic phases from ab initio and experiment, (2014).

[87] K. Miwa, A. Fukumoto, First-principles calculation of the structural, electronic, and vibrational properties of gallium nitride and aluminum nitride, Phys. Rev. B. 48 (1993) 7897–7902. doi:10.1103/PhysRevB.48.7897.

[88] C.P. Kempter, N.H. Krikorian, J.C. Mcguire, The crystal structure of yttrium nitride, J. Phys. Chem. 61 (1957) 1237–1238. doi:10.1021/j150555a023.

[89] M. Guemmaz, A. Mosser, J.J. Grob, Ion implantation processing of sub-stoichiometric titanium nitrides and carbonitrides: Chemical structural and micromechanical investigations, Appl. Phys. A Mater. Sci. Process. 64 (1997) 407–415. doi:10.1007/s003390050497.

[90] L. Gerward, J. Staun Olsen, U. Benedict, J.P. Itié, J.C. Spirlet, The crystal structure and the equation of state of thorium nitride for pressures up to 47 GPa, J. Appl. Crystallogr. 18 (1985) 339–341. doi:10.1107/s0021889885010421.

[91] R.A. Evarestov, A.I. Panin, A. V. Bandura, M. V. Losev, Electronic structure of crystalline uranium nitrides UN, U 2N3 and UN2: LCAO calculations with the basis set optimization, in: J. Phys. Conf. Ser., Institute of Physics Publishing, 2008. doi:10.1088/1742-6596/117/1/012015.

[92] S.M. Fatemi, M. Foroutan, Study of dispersion of carbon nanotubes by Triton X-100 surfactant using molecular dynamics simulation, J. Iran. Chem. Soc. 12 (2015) 1905–1913. doi:10.1007/s13738-015-0665-1.

[93] G. Wei, A. Rar, J.A. Barnard, Composition, structure, and nanomechanical properties of DC-sputtered CrNx (0≤x≤1) thin films, Thin Solid Films. 398 (2001) 460–464. doi:10.1016/S0040-6090(01)01388-8.

[94] A.R. Denton, N.W. Ashcroft, Vegards law, Phys. Rev. A. 43 (1991) 3161–3164. doi:10.1103/PhysRevA.43.3161.

[95] T. Sand, C. Geers, Y. Cao, J.E. Svensson, L.G. Johansson, Effective Reduction of Chromium-oxy-hydroxide Evaporation from Ni-Base Alloy 690, Oxid. Met. 92 (2019) 259–279. doi:10.1007/s11085-019-09935-9.

[96] V. Peres, L. Favergeon, M. Andrieu, J.C. Palussire, J. Balland, C. Delafoy, M. Pijolat, High temperature chromium volatilization from Cr2O3 powder and Cr2O3-doped UO2 pellets in reducing atmospheres, J. Nucl. Mater. 423 (2012) 93–101. doi:10.1016/j.jnucmat.2012.01.001.

[97] A.R. Massih, Effects of additives on uranium dioxide fuel behavior 2014:21 SSM perspective Background, 2014.

[98] A. Leenaers, L. De Tollenaere, C. Delafoy, S. Van den Berghe, On the solubility of chromium sesquioxide in uranium dioxide fuel, J. Nucl. Mater. 317 (2003) 62–68. doi:10.1016/S0022-3115(02)01693-8.

[99] C. Ganguly, R.N. Jayaraj, International Atomic Energy Agency., Indian Nuclear Society., Characterisation and quality control of nuclear fuels : (CQCNF-2002), Allied Publishers, 2004.

[100] K. Johnson, V. Ström, J. Wallenius, D.A. Lopes, Oxidation of accident tolerant fuel candidates, J. Nucl. Sci. Technol. 54 (2017) 280–286. doi:10.1080/00223131.2016.1262297.

[101] P.A. Demkowicz, J.L. Jerden, J.C. Cunnane, N. Shibuya, R. Baney, J. Tulenko, Aqueous Dissolution of Urania-Thoria Nuclear Fuel, Nucl. Technol. 147 (2004) 157–170. doi:10.13182/NT04-A3522.

[102] M. Jolkkonen, P. Malkki, K. Johnson, J. Wallenius, Uranium nitride fuels in superheated steam, J. Nucl. Sci. Technol. 54 (2017) 513–519. doi:10.1080/00223131.2017.1291372.

[103] T.W. Kerlin, B.R. Upadhyaya, Boiling water reactors, in: Dyn. Control Nucl. React., Elsevier, 2019: pp. 167–189. doi:10.1016/b978-0-12-815261-4.00013-5.